Geophysical Journal International

Geophys. J. Int. (2014) doi: 10.1093/gji/ggt522

Geophysical Journal International Advance Access published February 18, 2014

Space–time evolution of crustal deformation related to the M_w 6.3, 2009 L'Aquila earthquake (central Italy) from principal component analysis inversion of GPS position time-series

A. Gualandi,[1,3] E. Serpelloni[2] and M. E. Belardinelli[3]

[1] *Istituto Nazionale di Geofisica e Vulcanologia, Sezione di Bologna, Bologna, Italy. E-mail: adriano.gualandi@bo.ingv.it*
[2] *Istituto Nazionale di Geofisica e Vulcanologia, Centro Nazionale Terremoti, Bologna, Italy*
[3] *Dipartimento di Fisica e Astronomia, Settore di Geofisica, Università di Bologna, Bologna, Italy*

Accepted 2013 December 23. Received 2013 December 20; in original form 2013 January 11

SUMMARY

In this work, we present a study of the coseismic and post-seismic crustal deformation associated to the M_w 6.3, 2009 April 6 L'Aquila earthquake from the analysis of GPS displacement time-series. We use a principal component decomposition-based inversion method to study the space- and time-dependent evolution of slip on faults without any *a priori* assumption on the model used to characterize the temporal evolution of crustal deformation. The method adopted allows us to account for the initial post-seismic deformation in estimating the coseismic displacements, in a consistent manner for the whole GPS network. We use elastic dislocation theory and a least-squares procedure to invert for the slip distribution on the mainshock fault (Paganica fault) and a second fault (Campotosto fault), where a M_w 5.2 aftershock occurred on April 9. The geometries for these faults are obtained from a singular value decomposition of precisely relocated aftershocks. We find that the use of complex fault geometries is not justified by the GPS observations available. An inversion that accounts for post-seismic slip to occur on both the Paganica and Campotosto faults provides a better fit to the GPS time-series observations, than using only the Paganica fault segment, at a 95 per cent confidence level. Within our resolution, afterslip regions do not migrate over time and are localized on fault patches that are approximately complementary to those of coseismic slip. We find that the position of some relevant afterslip patches is different if the inversion is performed assuming a fixed rake or not. We estimate the parameter $a - b$ of rate- and state-dependent friction on those fault regions accommodating afterslip that are robustly characterized in our inversions. We find values of the order of 10^{-3}, which is near the transition from potentially unstable to nominally stable friction. These results are in agreement with laboratory measurements performed on typical rocks of the L'Aquila region.

Key words: Time series analysis; Space geodetic surveys; Seismic cycle; Transient deformation.

1 INTRODUCTION

The M_w 6.3 mainshock of the 2009 central Italy earthquake sequence occurred at 01:32 UTC of April 6 near the city of L'Aquila, causing 308 casualties and damages in a wide area of the Abruzzi region of central Italy. The 2009 seismic sequence included five events with $5 < M_w < 6$ and activated a NW–SE trending seismogenic volume expanding for nearly 50 km along the central Apennines (see Fig. 1). Here, both geological and geodetic observations indicate a regional NE–SW oriented extension, occurring at background rates of ∼2–3 mm yr^{-1} (Serpelloni *et al.* 2006; Faure *et al.* 2010; D'Agostino *et al.* 2011; Galvani *et al.* 2013). This extension is accommodated across a complex belt of subparallel NW–SE oriented normal faults, with lengths ranging from few to 15–20 km, mostly steeply dipping towards the SW (Barchi *et al.* 2000; Galadini & Galli 2000; Valensise & Pantosti 2001; Boncio *et al.* 2004).

Earthquake fault plane solutions (Pondrelli *et al.* 2010; Scognamiglio *et al.* 2010; Herrmann *et al.* 2011), space geodetic observations (Anzidei *et al.* 2009; Atzori *et al.* 2009; Walters *et al.* 2009; Cheloni *et al.* 2010; Devoti *et al.* 2012; Serpelloni *et al.* 2012) and aftershock distribution (Chiarabba *et al.* 2009; Chiaraluce *et al.* 2011) have consistently shown that the largest shocks of the sequence ruptured a set of shallow, SW-dipping, normal faults, running roughly parallel to the NW–SE trending Apennines belt, which are intermediate between the eastern and western fault systems described in Galadini & Galli (2000). The April 6 M_w 6.3

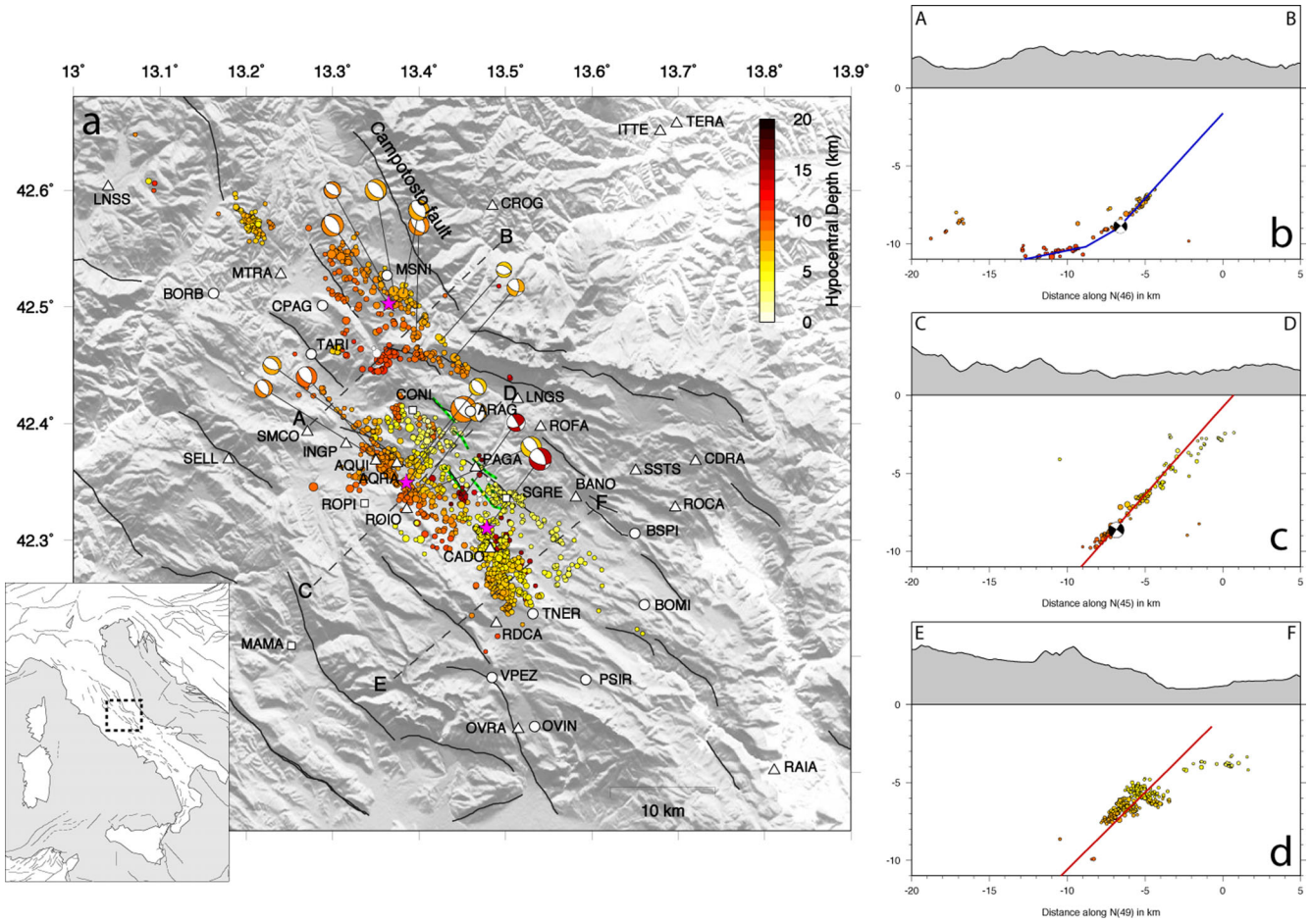

Figure 1. (a) Map of the region involved in the seismic sequence. Coloured circles are the aftershocks from Chiaraluce *et al.* (2011), beach balls are the focal mechanisms from Pondrelli *et al.* (2010) and purple stars indicate the mainshock (April 6, lon 13.39°, lat 42.35°, depth 8.6 km) and the two most relevant aftershocks (April 7, lon 13.48°, lat 42.31°, depth 14.2 km; April 9, lon 13.36°, lat 42.50°, depth 8.9 km). GPS stations are also shown. White circles/squares indicate those stations that have been used only for the coseismic/post-seismic analysis. White triangles indicate the stations used in both coseismic and post-seismic study. Black lines are the active faults from Boncio *et al.* (2004) and Galli *et al.* (2008). Green dashed lines are the observed surface ruptures after the mainshock from Boncio *et al.* (2010). Black dashed lines are the sections reported in panels (b), (c) and (d). (b) Section A–B of panel (a). The focal mechanism corresponds to the April 9 aftershock. The blue line is the section of the geometry C2 (see Table 1). (c)–(d) Sections C–D and E–F of panel (a). The focal mechanism (c) represents the mainshock. Red lines are the sections of geometry P4 (see Table 1).

mainshock was followed, on April 7, by a M_w 5.4 aftershock, located about 15 km SE from the mainshock and at a hypocentral depth of ∼15 km, and, on April 9, by a M_w 5.2 aftershock (at hypocentral depth of 9 km), occurred on a secondary fault segment, the Campotosto fault, located NW of the mainshock (Chiaraluce *et al.* 2011). The Campotosto fault was also later struck, on June 22, by a M_w 4.4 aftershock, at a hypocentral depth >10 km.

Space geodetic observations (GPS and InSAR) recorded significant post-seismic deformation over a wide area, extending >30 km from the epicentre, the months after the mainshock (Lanari *et al.* 2010; D'Agostino *et al.* 2012; Devoti *et al.* 2012). Cheloni *et al.* (2010) and D'Agostino *et al.* (2012) modelled the post-seismic surface displacements as due to afterslip on the Paganica fault plane, assuming that the post-seismic deformation of GPS observations evolves with time following an exponential decay function, as in Lanari *et al.* (2010) and Devoti *et al.* (2012). Cheloni *et al.* (2010) and D'Agostino *et al.* (2012) found that afterslip has not fully propagated to the surface but mostly occurred at a shallow depth, between the main coseismic patch and the surface, with the post-seismic slip that appears to encircle the main coseismically slipping portion of the Paganica fault.

All previous works are based on at least one of these two assumptions: (1) surface displacements evolve in time following an exponential decay function, and (2) only the Paganica fault, parametrized as a simple rectangular plane, accommodates post-seismic afterslip. Here, we propose a new study of the co- and post-seismic crustal deformation where these two assumptions are relaxed. We explore more complex fault geometries (see Section 2), as derived from precisely relocated aftershocks, and we model the observed surface displacements, detected by GPS observations (see Section 3), without any *a priori* assumptions on the temporal evolution of crustal deformation (see Section 4). In order to achieve this goal, different methods have been recently developed (e.g. Hsu *et al.* 2007; Hetland *et al.* 2012). Here, we perform the space- and time-dependent deformation analysis by means of the principal component analysis-based inversion method (PCAIM; Kositsky & Avouac 2010), which allows us to invert for slip on faults with assigned geometry under the assumption that this is the main cause of the observed deformation field.

In addition to afterslip, other processes can be invoked to explain post-seismic deformation, such as viscoelastic relaxation and poroelastic rebound (e.g. Barbot & Fialko 2010 and references therein).

Each process gives a different signature in the observed temporal and spatial evolution of post-seismic deformation. All processes tend to relax over time, and they are characterized by different decay constants. In this work, we do not take into account the viscoelastic relaxation process since its typical decay times (∼10 yr) are much greater than the time interval spanned by our post-seismic data (e.g. Pollitz *et al.* 2008; Suito & Freymueller 2009; Viti *et al.* 2012). We also neglect the poroelastic mechanism and verify *a posteriori* the validity of such an assumption (see Section 6). Besides these three processes, also aftershocks contribute to post-seismic relaxation (Rice & Gu 1983), even if the detectability of their effect on surface displacements depends on their magnitude and depth. Moreover, Fielding *et al.* (2009) pointed out the possibility to explain the near-fault post-seismic deformation, particularly observed by InSAR data, through dilatancy recovery. The spatial density of our data set, however, does not allow us to detect such a signal. Afterslip models explain properly the observations ($\chi^2_r < 1$, see Section 6), and we do not need to take into account the effects of fault-zone dilatancy recovery to fit the data.

The PCAIM method has been tested and validated both on synthetic and real post-seismic data (e.g. Kositsky & Avouac 2010; Perfettini *et al.* 2010) for seismic events of magnitude larger than 7, but its application to moderate earthquakes is still unexplored. This last consideration together with the density of the GPS network in the epicentral region motivate us in: (i) testing PCAIM concerning the distribution of coseismic and post-seismic faults slip, in comparison with previously obtained solutions (see Sections 4–6), and (ii) investigating implications on the mechanics of faulting during the L'Aquila sequence (Section 7).

A better understanding of the physical processes that control the relative amount and location of seismic and aseismic sliding is a key goal in the study of fault mechanics. Rate- and state-dependent friction allows a fault to develop both seismic instabilities and aseismic sliding, according to the value of the constitutive and mechanical parameters (e.g. Rice & Gu 1983). Geodetic data recording coseismic and post-seismic deformation allow us to infer information about the frictional properties of fault planes involved in a seismic sequence (e.g. Hsu *et al.* 2006; Fukuda *et al.* 2009; Perfettini *et al.* 2010). While most of destructive earthquakes in Italy nucleate within, or propagate through, thick sequences of carbonate, particularly along the Apennines, little is known about the frictional properties of these rocks. Few laboratory experiments have been performed to determine the rate- and state-dependent frictional properties of carbonate rocks (e.g. Scuderi *et al.* 2013 and references therein). Moreover, there are few applications of rate–state and state–state friction to study afterslip following moderate-magnitude earthquakes (e.g. Johnson *et al.* 2006), and particularly on normal faults. In this work, we use the post-seismic faults slip evolution inverted by GPS observations to constrain a rate- and state-dependent friction model of afterslip. In particular, we estimate a range of variability of the frictional parameter $a - b$. In previous studies of the L'Aquila earthquake such an estimate was not possible because post-seismic observations were modelled assuming a temporal dependence different from that predicted by models of afterslip with rate- and state-dependent friction.

2 DETERMINATION OF FAULT MODEL GEOMETRIES

In previous studies, different geometries for the mainshock fault had been determined inverting for the coseismic displacements recorded by space geodetic data (e.g. Anzidei *et al.* 2009; Walters *et al.* 2009; Cheloni *et al.* 2010; Devoti *et al.* 2012; Serpelloni *et al.* 2012), and all of the coseismic slip distributions had been determined on a simple planar fault. On the other hand, precise relocations of aftershocks (Chiaraluce *et al.* 2011; Valoroso *et al.* 2013) provide evidence that the L'Aquila sequence evolved on a more complex fault system, characterized by major and secondary fault planes, where the two major faults are the Paganica fault and, northwest of it, the Campotosto fault, forming a NW-trending en echelon system ∼50 km long. The ∼16 km long Paganica fault shows a rather well-defined planar geometry, with a constant dip (∼48°) down to 10 km depth, in its central and northern portions, thus justifying the assumptions of planar faults in geodetic inversions. However, the Paganica fault shows a more complex and broader distribution of aftershocks in its southern portion (see Figs 1c and d). The Campotosto fault, activated by three events with $5.0 \leq M_w \leq 5.2$, shows a listric geometry, composed by planar segments with different dips along depth rather than a smoothly curving single fault surface (Chiaraluce *et al.* 2011; see Fig. 1b). No records of coseismic deformation associated to these aftershocks have been observed in the geodetic observations.

Here, we exploit the relocated aftershock catalogue of Chiaraluce *et al.* (2011) to define a suite of fault model geometries for the Paganica and Campotosto faults to be used in the coseismic and post-seismic slip inversions. We test the sensitivity of GPS observations to the use of increasingly complex fault geometries (see Section 5), adopting as a benchmark for the Paganica fault its geodetic solution (i.e. from Serpelloni *et al.* 2012). The fault geometries are obtained with the following procedure: (1) we identify spatial clusters from the relocated aftershocks by applying a *k*-means algorithm, therefore, each cluster is defined by a cloud of points; (2) we determine the plane that best approximate the cloud of points through a singular value decomposition method. This technique allows us to estimate the strike and dip angles of the planes, provided that the number of clusters is already identified (see Section S1), minimizing the degree of subjectivity in tracing fault geometries from aftershock catalogues. In order to constrain the absolute position of the fault planes, we force the shallowest segments to cut the Earth's surface in correspondence of traces of active faults recognized in the field (e.g. Boncio *et al.* 2010).

Our results are shown in Table 1, where we report also the geometry derived by Serpelloni *et al.* (2012), called P1, which is assumed as representative of the geodetically derived geometry of the Paganica fault. The geometries derived from the aftershocks catalogue are the following (see also Fig. S1): (P2) one rectangular plane derived from the northern Paganica seismic cluster; (P3) one rectangular plane derived from the whole seismicity near the Paganica fault; (P4) two rectangular planes, for the northern and southern clusters of the Paganica seismicity. The orientation of these planes shows a narrow variation: 45°–48° for the dip angle and 134°–142° for the strike angle, in agreement with the ranges of values suggested by geodetic data and focal mechanisms (42°–56° for the dip angle and 126°–144° for the strike angle, see table 1 in Serpelloni *et al.* 2012).

Aftershocks on the Campotosto fault occurred at depths greater than 6 km and show a subhorizontal distribution at a depth greater than 10 km (Fig. 1b). The geometries derived to approximate the Campotosto fault are (see Table 1 and Fig. S1): (C1) one rectangular plane and (C2) three rectangular planes with variable dips along depth. In order to determine the one plane approximation for the Campotosto fault (C1), among the three planes of the C2 geometry we choose the parameters of the shallowest plane containing the most relevant aftershock, namely, the April 9 M_w 5.2

Table 1. Fault geometries obtained from the analysis of the relocated catalogue of aftershocks (Chiaraluce *et al.* 2011). P1 is the geometry obtained by Serpelloni *et al.* (2012) inverting GPS displacements. P2, P3 and P4 are derived by relocated aftershocks. The Campotosto geometries (C1 and C2) are also reported in the table. Last line is referred to the April 9 aftershock. It shows the localization of the aftershock (longitude, latitude and depth) and the orientation of the two conjugate planes of the focal mechanism (strike and dip) from Pondrelli *et al.* (2010). The strike and dip angles of the second conjugate plane are in good agreement with the values obtained for the shallowest Campotosto plane (C1 or first line of C2).

Name	Length (km)	Width (km)	$Depth_{top}$ (km)	$Depth_{bott}$ (km)	Dip (°)	Strike (°)	$Lon_{mid\text{-}point}$ (E°)	$Lat_{mid\text{-}point}$ (N°)
P1	30	25.1	0	19.4	50.5	129.4	13.35	42.25
P2	30	24	0	17.9	48.4	134.3	13.34	42.26
P3	30	24	0	18.0	47.3	141.6	13.33	42.26
P4	14	24	0	16.9	44.7	139.7	13.39	42.19
	18	24	0	18.0	48.4	134.3	13.29	42.29
C1	18	18	0.5	13.8	47.5	136.2	13.33	42.46
C2	18	10	1.6	9.0	47.5	136.2	13.37	42.49
	18	2.4	9.0	10.2	30.1	136.2	13.35	42.48
	18	6	10.2	11.4	11.4	136.2	13.30	42.45
Aftershock April 9	Lon (°)	Lat (°)	Depth (km)	Strike 1 (°)	Dip 1 (°)	Strike 2 (°)	Dip 2 (°)	
Focal mechanism	13.36	42.50	8.888	329	45	136	46	

(Fig. 1b). Otherwise, we would evidently underestimate the dip of the whole structure, violating also the geological constraints derived from surface evidences of active faulting (Boncio *et al.* 2010). The plane determined using the shallowest seismicity or the C1 geometry shows strike (136.2°) and dip (47.5°) angles that are in good agreement with one of the two conjugate planes derived from the study of the focal mechanism (Pondrelli *et al.* 2010; 136° and 46°; see Table 1).

3 GPS OBSERVATIONS

We use displacement time-series obtained from the analysis of the GPS data collected at both continuous (cGPS) and survey mode (sGPS) networks (see Devoti *et al*. 2012 and Serpelloni *et al.* 2012 for a more comprehensive description of the networks and quality of data used). Table S1 shows the occupation history of the GPS stations used in this work. The raw GPS phase data have been processed following the same three-steps procedure described in Serpelloni *et al.* (2012), to which we refer for a more detailed description of the data analysis strategy used to derive the position time-series. It is known that GPS time-series contain various systematic errors (from network common to site-dependent) and random errors (e.g. Williams 2003; Dong *et al.* 2006; Langbein 2008). In regional network analysis, the so-called common mode error (CME) is one of the major spatially correlated error sources, which is mitigated through a technique commonly referred to as regional filtering. The 'stacking' approach (Wdowinski *et al.* 1997), commonly used in regional analysis, assumes that the CME is spatially uniform, which is a good approximation for small networks, but as the spatial extent increases, the assumption is no longer valid (e.g. Márquez-Azúa & DeMets 2003). Here, we use a principal component analysis (PCA) technique (Dong *et al*. 2006), which decomposes the network time-series into a set of temporally varying (principal component) modes. Each mode consists of a common temporal function and related different spatial response, providing a mathematical framework to perform spatiotemporal filtering. This approach allows us to remove the assumption of spatially uniform distribution, letting the displacement data reveal the spatial distribution of the CME. The PCA method is applied on the residual time-series (detrended and cleaned for instrumental offsets, seasonal signals and outliers) of ∼650 cGPS stations distributed over a wider region, encompassing the Euro-Mediterranean area (Serpelloni *et al.* 2013), while excluding stations in central Italy, likely affected by post-seismic deformation. We assume the first and second Principal Components (PCs) to be representative of the CME, accounting for more than 50 per cent of the total variance. By filtering the time-series from the estimated CME we obtain ∼35 per cent and ∼30 per cent reduction of the weighted root mean squares (WRMS) values in the horizontal and vertical components, respectively, with a significant gain in the signal-to-noise ratio of the post-seismic displacements transient. This is particularly important for studying smaller amplitude crustal deformation related to moderate magnitude earthquakes.

The input time-series of the coseismic and post-seismic deformation analysis, described in the next section, are the CME filtered, detrended time-series, which are obtained after removing a constant velocity term, a seasonal (annual + semi-annual) term and any non-tectonic offset due to changes in the stations equipment configurations. For those stations for which no reliable pre-earthquake interseismic velocities can be determined (e.g. because only post-earthquake data are available or only a short time interval before the earthquake is available), we constrained their velocities to *a priori* values obtained from a least-squares interpolation of the 3-D velocity field of central Italy (Galvani *et al.* 2013; Serpelloni *et al.* 2013). For estimating the coseismic displacements we limited our analysis to the first 11 d after the mainshock, in order to include as much GPS stations as possible. We use the time-series of 67 stations, belonging to both cGPS and sGPS networks. For those sGPS stations that have no data at least in the 5 d before the mainshock we assume a position around 0 and estimate the uncertainty propagating the errors on the velocity and the position at the reference epoch. To study the post-seismic deformation we use the detrended and filtered time-series of 27 GPS stations that recorded continuously after the mainshock. The GPS data analysis carried out enables us to obtain the post-seismic slip history with 1-d resolution, that is, a much higher degree of detail than the one allowed by InSAR measurements. Such a high temporal resolution allows us to look for fast post-seismic transients in the first weeks after the mainshock.

4 INVERSION METHOD

In order to study the space and time distribution of coseismic and post-seismic slip on the fault planes activated during the seismic sequence, we invert GPS displacement time-series by means of the PCAIM software (Kositsky & Avouac 2010), developed at the California Institute of Technology (Caltech). The displacement

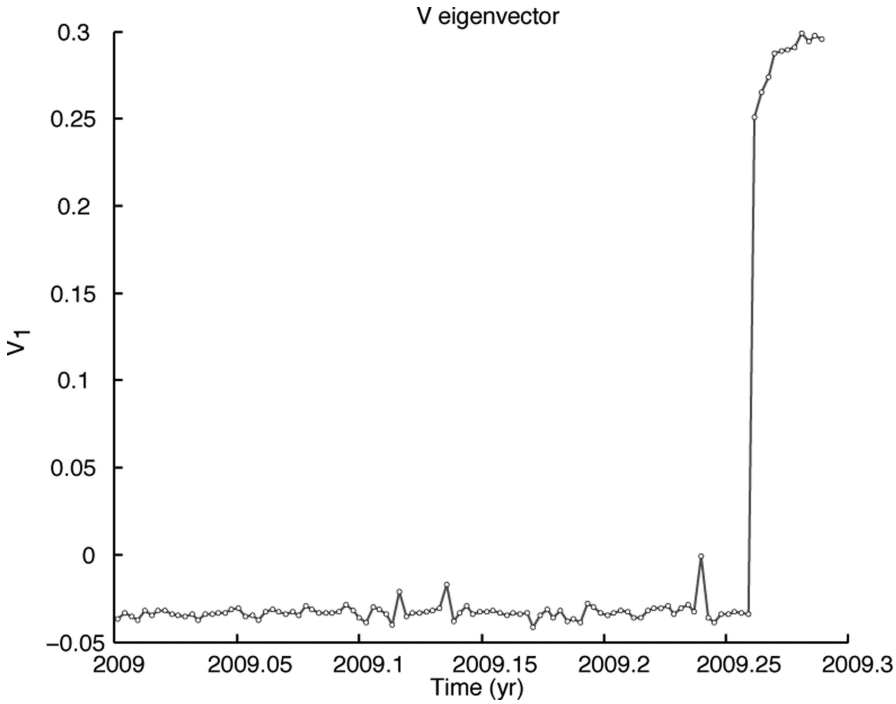

Figure 2. Temporal eigenvector for the coseismic decomposition. To make a realistic estimation of the coseismic offset considering also stations that missed data immediately after the mainshock it is necessary to retrieve by decomposition the early post-seismic displacement (the last 11 d shown in the figure).

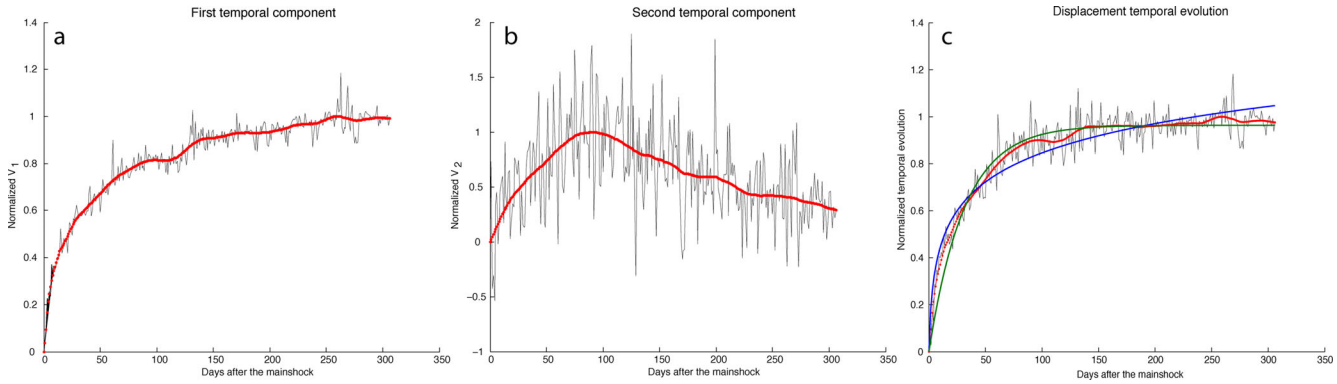

Figure 3. (a)–(b) First and second temporal eigenvectors for the post-seismic decomposition. Red lines are obtained filtering high-frequency signal. (c) The red line is the displacement temporal evolution for the post-seismic decomposition, evaluated as the weighted sum of the eigenvectors, where the weights used are the correspondent eigenvalues (the elements of matrix S in eq. S2). The blue line is the best logarithmic fit and the green line is the best exponential fit. The best parameters estimated with an unconstrained non-linear minimization of the sum of squared residuals (SSR) are: $A_{\log}\sim0.18$, $\tau_{\log}\sim0.94$ d, $A_{\exp}\sim0.96$, $\tau_{\exp}\sim31.2$ d.

signal is decomposed into its principal components and the spatial part of the principal components are inverted as if they were actual displacements (see Section S2.1). As a consequence, the common pattern of the displacements to be inverted is retrieved directly from GPS observations, rather than from *a priori* assumptions. Here, we have also used the PCAIM code to estimate the coseismic displacements, while accounting for early post-seismic transients, and invert for the coseismic slip distribution.

Let us organize the observed time-series in a matrix of size $m \times n$, where each row corresponds to the time-series from one component (east, north or vertical) at one station and each column corresponds to all data measured at a given epoch, and let us call this matrix the data matrix ($X_{\rm dat}$). The first step of the PCAIM analysis consists in decomposing $X_{\rm dat}$, and determine the number (r) of principal components to be used in order to reproduce the observed GPS displacement time-series (for details see Section S2.1). In a first step, the removal of outliers from the time-series is done efficiently using one component (for details see Section S2.2). However, the one component decomposition does not always reproduce appropriately the original displacement data. Unfortunately, there is not a well-defined procedure to determine the number of sufficient components. Following Kositsky & Avouac (2010), we use a χ^2 test and an F-test. The former suggests that one component ($r = 1$) is sufficient to explain our GPS displacement time-series. Instead, adopting an F-test as a criterion, we conclude that adding a second component better explain the data at a 95 per cent confidence level. As described in Section S2.3, we decide to use one component for the coseismic study (Fig. 2) and two components for the post-seismic modelling (Fig. 3).

After the choice of r, the slip inversion is performed on the spatial part of the data matrix (see eq. S3). We consider dislocations embedded in an elastic and homogeneous half-space, with a Poisson's

Table 2. Statistical results for the co- and post-seismic inversions using the different geometries defined in Table 1. The value of γ is established through a L-curve method, and the value R is a compromise between the fixed ($R\rightarrow\infty$) and completely variable ($R = 1$) rake configurations. ρ, χ^2, $\chi_r{}^2$, WRMSE and WRMSE_{14} are described in the main text. We indicate two values of rake in the fixed range configuration ($R\rightarrow\infty$) of geometry P4 because in this configuration we have two fault segments, as specified in the main text and Table 1.

	Coseismic			Post-seismic						
Name	R	γ (cm^{-1})	Stn $\rho > 3$ (%)	R	γ (cm^{-1})	χ^2	$\chi^2{}_r$	WRMSE (cm)	WRMSE_{14} (cm)	Rake range (°)
P1	1	5	5	1	2.5	11 879	0.7632	20.4841	23.6683	0 ÷ –180
P2	1	5	4	1	2.5	11 738	0.7542	20.3927	23.2194	0 ÷ –180
P3	1	5	6	1	2.5	12 000	0.7710	20.7317	24.8426	0 ÷ –180
P4	1	5	4	1	2.5	11 636	0.7488	20.3698	23.1253	0 ÷ –180
P1	20	5	7	15	2.5	12 191	0.7833	20.6898	24.3893	–89 ÷ –168
P2	15	7	5	15	2.5	12 245	0.7868	20.7520	24.7297	–90 ÷ –140
P3	10	5	7	15	2.5	12 506	0.8035	21.0131	25.7733	–89 ÷ –119
P4	15	5	5	15	2.5	12 513	0.8052	20.9332	25.5800	–91 ÷ –119
P1	∞	4000	10	∞	25	14 081	0.9047	21.3392	26.9896	–90
P2	∞	3500	8	∞	25	13 398	0.8608	21.2078	26.3628	–90
P3	∞	3500	7	∞	25	13 409	0.8616	21.2071	26.5186	–90
P4	∞	2500	9	∞	20	15 097	0.9715	21.8815	29.0663	–81; –90

ratio of 0.25. The Green's functions are then computed from the solutions of Okada (1985). In our inversions, we discretized the fault planes with $2 \times 2\,\mathrm{km}^2$ rectangular patches. Since we have to manage with an ill-posed linear problem, the slip inversion problem has to be regularized. In order to achieve this goal, we use a Laplacian operator, where the weight associated to the regularization is driven by a parameter (γ), which is defined using the L-curve method for both coseismic and post-seismic slip inversions. For more details see Section S2.4.

5 GEOMETRY SELECTION AND RAKE CONSTRAINTS

With the goal of investigating the sensitivity of the available GPS observations with respect to the use of different fault geometries, of increasing complexity, we test all the geometries proposed in Section 2, while inverting both the coseismic and post-seismic displacements. In the coseismic case, for each geometry of Table 1, we evaluate the difference between the offsets calculated with the modelled time-series and the decomposed ones (Δoffset). In order to figure out the goodness-of-fit of the coseismic displacements, we estimate the ratio $\rho = \Delta\mathrm{offset}/\sigma_{\mathrm{dec}}$ for each time-series, where σ_{dec} is the error associated to the offset deduced from the decomposition of the observations. For the post-seismic phase we estimate the χ^2, the reduced χ^2 and the WRMS error (WRMSE) statistics, defined as follow:

$$\chi^2 = \sum_{i=1}^{m}\sum_{j=1}^{n} \frac{(X_{\mathrm{mod}}(i,j) - X_{\mathrm{dat}}(i,j))^2}{\sigma(i,j)^2},$$

$$\chi_r^2 = \frac{\chi^2}{N - r(n+m+1)},$$

$$\mathrm{WRMSE} = \sum_{i=1}^{m} \sqrt{\frac{\sum_{j=1}^{n} \frac{(X_{\mathrm{mod}}(i,j) - X_{\mathrm{dat}}(i,j))^2}{\sigma(i,j)^2}}{\sum_{j=1}^{n} \frac{1}{\sigma(i,j)^2}}},$$

where X_{mod} is the modelled matrix (see eq. S4 in Section S2.1), X_{dat} is the data matrix with the corresponding 1-sigma uncertainty σ and N is the total number of data, that is the total number of recorded displacements in the GPS time-series. We also compute the WRMSE_{14}, corresponding to the WRMSE calculated for the first 14 d after the mainshock (see Table 2), during which the fastest post-seismic transients are measured.

For each Paganica fault geometry, we invert the position time-series in order to obtain the coseismic and post-seismic slip distributions. At this stage we test several assumptions about the rake of the inverted slip, and evaluate how these assumptions affect the slip distributions. We perform the inversions assuming three different configurations for the rake: (i) completely variable, (ii) completely fixed along the dip direction (–90°) and (iii) slightly variable around the dip direction. The application of these three different constraints is achieved by adopting different weights to the along-strike and along-dip components of the Laplacian operator, whose ratio is indicated by R. When this ratio is equal to 1, the rake can assume any value, thus corresponding to a completely variable rake configuration, with only the positivity constraint imposed to avoid thrust slip. Increasing the value of R forces the solution to have rake values closer to –90°. To perform a fixed rake inversion we do not use the R parameter, but we still denote this configuration with the symbol $R\rightarrow\infty$. For further details on the selection of the intermediate R values, see Section S2.5. In Table 2, we show, for each geometry of Table 1, the ranges in which the rake varies, and the corresponding statistical results.

For both the coseismic and post-seismic cases, a higher variability in the ability of explaining the observations is obtained by varying the assumptions about the rake, or the value of R (see Table 2). For the same rake assumption, the difference in the fit of the post-seismic observations between two different geometries is not relevant and the relative gain in the reduced χ^2 between the worst and the best-fit geometry is ∼2–3 per cent. The only exception is in case of a fixed rake inversion ($R\rightarrow\infty$), which is not suitable for the geometry P4 because the code allows us to assign a rake value of –90° only to one segment (the rake of the second segment is assigned assuming a horizontal component of the slip vector with the same direction as the first segment). For the same geometry, we find that we can significantly better fit the displacement time-series assuming a variable rake ($R = 1$), without fixing it to an *a priori* value. For example, considering the simplest geometry derived from the seismic catalogue (P2), for the post-seismic case we have a gain of ∼12 per cent in the reduced χ^2 statistic, passing from a fixed rake ($R\rightarrow\infty$) to a variable one ($R = 1$).

We conclude that increasing the complexity of fault geometries, as defined from the aftershock distribution in Section 2, is not

Table 3. Statistical results for the post-seismic inversion taking into account the P2 geometry for the Paganica fault and the two different geometries of Campotosto, as defined in Table 1. C1 is the one-plane model and C2 is the three planes one. The value of γ for the Campotosto fault is established through a L-curve method, and the value $R = 15$ is a compromise between the fixed ($R \to \infty$) and completely variable ($R = 1$) rake configurations. The values of γ and R corresponding to the Paganica fault (P2) are the ones derived from the inversion with only Paganica (Table 2). χ^2, ${\chi_r}^2$, WRMSE and WRMSE_{14} are described in the main text.

Name	R	γ (cm^{-1})	χ^2	${\chi^2}_r$	WRMSE (cm)	WRMSE_{14} (cm)
P2	1	2.5	11 462	0.7442	20.2112	22.2231
C1	1	2				
P2	15	2.5	11 995	0.7788	20.5843	23.7855
C1	15	2				
P2	1	2.5	11 433	0.7423	20.1893	22.0279
C2	1	2				
P2	15	2.5	11 956	0.7763	20.5601	23.5427
C2	15	2				

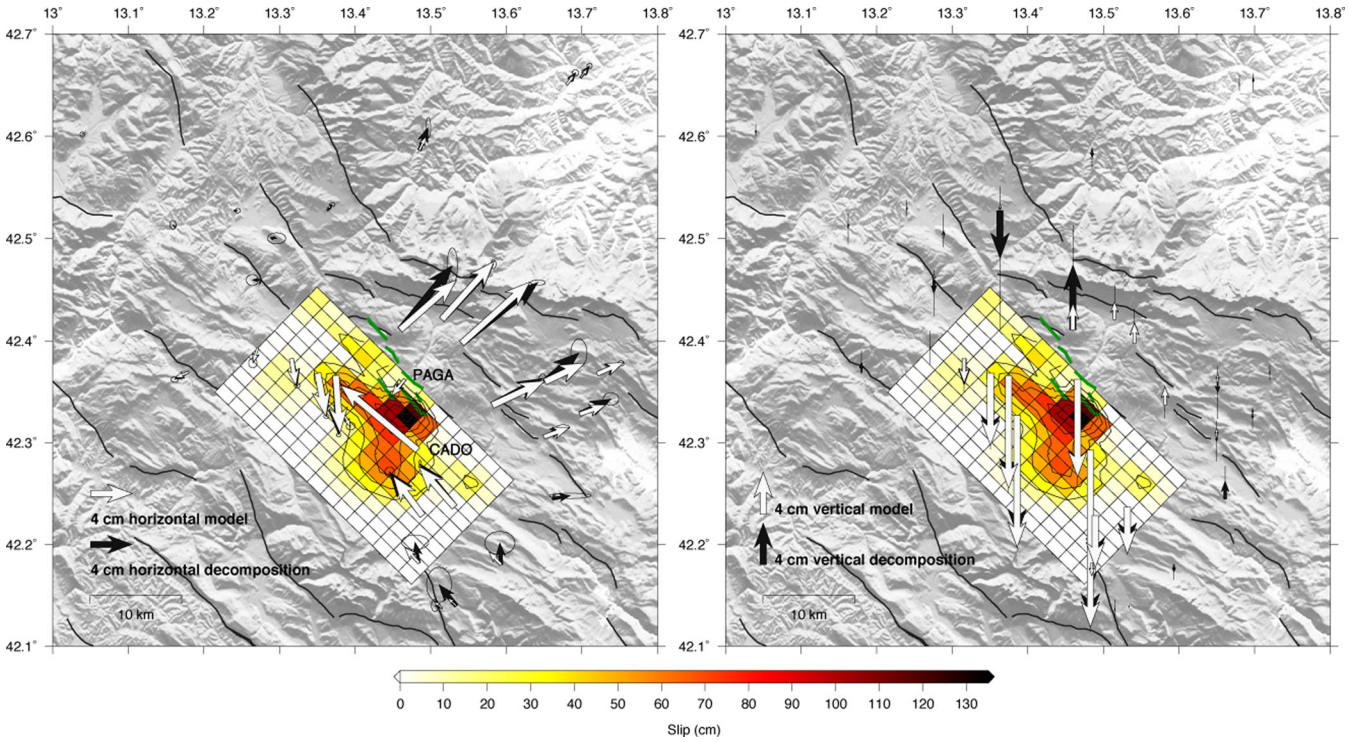

Figure 4. Coseismic slip model. Black and green lines are the same of Fig. 1. Contouring lines indicate coseismic constant slip regions starting from 20 cm to the maximum value, stepping every 20 cm. Left and right panels show horizontal and vertical displacements, respectively, for the stations used in the inversion. The slip and the displacements are computed as the value of the day after the mainshock less the value of the day before.

justified by the GPS observations available. Accordingly, we adopt the simplest geometry for the Paganica fault, namely, the P2 defined by one rectangular plane derived from the northern Paganica seismic cluster (Fig. S1).

As regards the Campotosto fault, since we do not observe coseismic GPS displacements relative to the largest April 9 aftershock, the use of relocated aftershocks for defining the fault model geometry is mandatory. However, also for the Campotosto fault we find that increasing the complexity of the fault geometry for the same value of R does not improve significantly the fit to the post-seismic time-series. This can be seen in Table 3 comparing results corresponding to lines 1 and 3 or 2 and 4. In the following, the geometry C1 will be used to model the Campotosto fault.

6 SLIP DISTRIBUTIONS: RESULTS

The inversions of coseismic and post-seismic GPS displacements with the P2 geometry provide the slip distributions shown in Figs 4 and 6. The smoothing weights (γ) and the range of rake variability are reported in Table 2. For the coseismic slip inversion, fixing the rake causes the number of not well-reproduced stations to be twice than adopting a variable rake solution (see Table 2). Allowing the rake to vary, and using $\gamma = 5\,\text{cm}^{-1}$, the coseismic slip distribution shows a maximum slip value of ~133 cm, confined between 4 and 6 km of depth downdip. Assuming a rigidity modulus of 30 GPa, it is equivalent to a seismic moment $M_0 = 3.1 \times 10^{18}$ N·m, which is in agreement with previous studies (e.g. Cheloni *et al.* 2010;

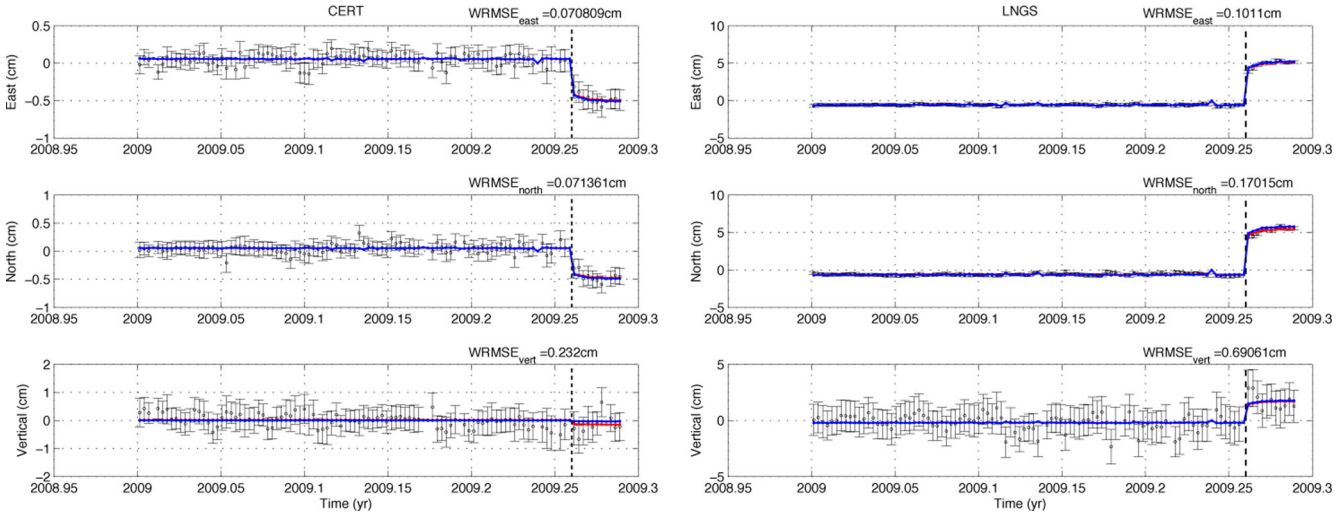

Figure 5. Position time-series of the GPS stations CERT (left) and LNGS (right). Black circles indicate the daily positions of the stations (X_{dat}) and black bars are the associated errors. Red lines are the time-series representation after the decomposition ($X_{dec} = USV^T \approx X_{dat}$). Blue lines are the modelled time-series ($X_{mod} = GLSV^T$). The dashed lines are mainshock markers. The WRMSE values are the weighted root mean square errors calculated between the decomposed and modelled time-series.

D'Agostino *et al.* 2012; Serpelloni *et al.* 2012), and corresponds to an earthquake of moment magnitude $M_w = 6.3$.

In Fig. 4, the modelled and observed coseismic displacements of the near-field stations are also shown. The estimated coseismic displacements are reported in Tables S2–S7. In Fig. 5, we show two examples of displacement time-series, in order to compare the original data with the decomposed and modelled time-series. Since we are using daily observations, our coseismic offset likely contains also some post-seismic deformation, developed in the first hours after the mainshock. However, we still refer to this offset as coseismic in the following of the paper. The coseismic slip distributions are available in the format of the Finite-Source Rupture Model Database, and can be downloaded at http://equake-rc.info/SRCMOD/.

The results of the coseismic slip inversion can be used to investigate the possible contribution from poroelastic rebound after the mainshock, and verify the validity of the assumption that afterslip is the main ongoing aseismic process during the post-seismic phase. We invert the coseismic surface displacements assuming an undrained value for the Poisson's modulus $\nu = 0.33$, and estimate the model displacements at the surface. Then, from the inverted coseismic slip distribution we evaluate the surface displacements assuming a drained value of the Poisson's modulus $\nu = 0.2$. Assuming no slip variation during the post-seismic phase, the difference between the model displacements in the drained case with respect to the undrained case can be considered as an estimate of the poroelastic rebound effect on post-seismic displacements. We find that this effect is relatively small, with maximum displacement amplitudes <2 cm, justifying our assumption of neglecting poroelastic deformation.

All the rake configurations adopted in our post-seismic inversions reveal a reduced χ^2 less than 1 (see Table 2). Nevertheless, we find that assuming a fixed rake provides the worst fit to the cumulative displacements (Figs 6e and f) and to the displacement time-series of three near-field key stations (CADO, RDCA, SGRE; see Fig. 7). If we look at the cumulated post-seismic horizontal displacements of CADO, RDCA and SGRE stations, we find that they all coherently show a northward motion that cannot be explained simply by a normal slip component. On the other hand, assuming a completely variable rake, we find that the best postseismic solution shows some shallow patches presenting a pure strike-slip component (Fig. 6b), in contrast with the observed focal mechanisms during the sequence (e.g. Pondrelli *et al.* 2010). Limiting the rake variability (using $R = 15$, see Section S2.5), our best solution (Figs 6c and d) is characterized by a maximum afterslip of $\sim$40 cm, confined between 6 and 10 km depth, downdip. For a rigidity modulus of 30 GPa, the total equivalent seismic moment released by afterslip, in the first 306 d after the mainshock, is $\sim 9.2 \times 10^{17}$ N·m. Such a value corresponds to an earthquake of moment magnitude $M_w \sim 5.9$. The afterslip on the Paganica fault plane does not spatially migrate over time, within the resolution of our observations, as also suggested in D'Agostino *et al.* (2012).

Differently from previously published works, here we investigate the possibility that also the Campotosto fault accommodated aseismic slip after the April 6 mainshock. By inverting the GPS time-series for afterslip on both the Paganica and Campotosto faults, we find a better fit to the displacement time-series, and particularly at GPS stations near the Campotosto fault, as shown in Fig. 8. Fig. 9 shows the post-seismic slip distribution obtained adding the Campotosto fault in the inversion. The afterslip distribution on the Paganica fault is affected by the introduction of the Campotosto segment, showing a variation in the afterslip module of more than 50 per cent (i.e. up to 8 cm) in the shallowest part of the northern Paganica fault segment, that is the closest to the Campotosto fault.

We calculate the model resolution matrix as in Du *et al.* (1992). If the resolution matrix is equal to the identity matrix, then each model parameter is uniquely determined. We obtain diagonal values of the resolution matrix <0.4 at depths greater than 2 km downdip, and <0.1 at depths greater than 10 km downdip. In all the post-seismic inversions, afterslip occurs on two main areas of the Paganica fault plane, located SE and NW of the main coseismic slip patch. We refer to them as region A and B, respectively (Figs 9 and 10a). In particular, the afterslip patches around region A are stably located on the same position of the fault plane in inversions obtained with different rake constraints. On the contrary, the location of region B varies adopting different rake constraints. We interpret this result considering the afterslip region A as a robust feature of our inversion, and a necessary condition to explain our GPS observations.

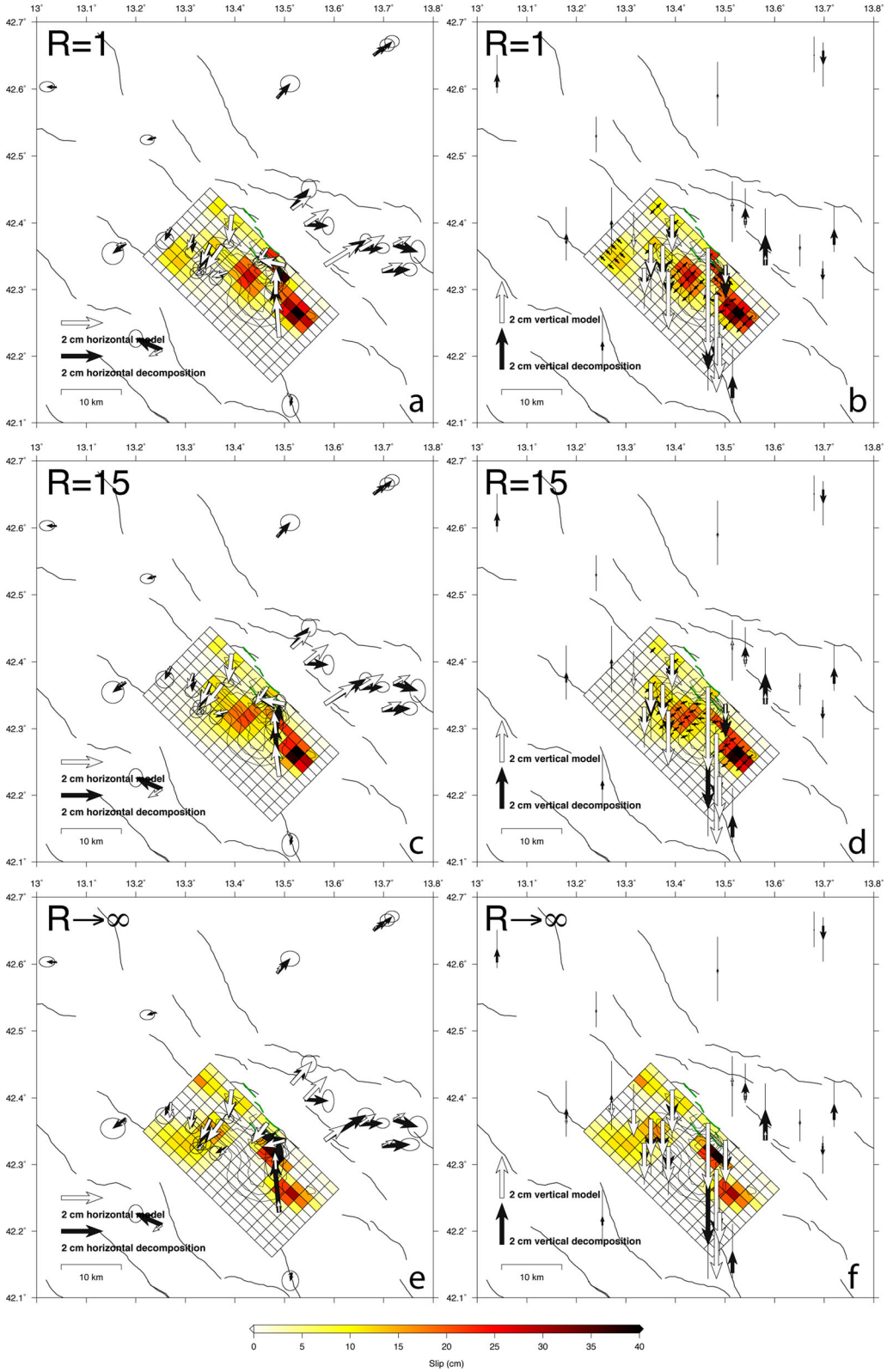

Figure 6. Post-seismic slip models. Black and green lines are the same of Fig. 1. Contouring lines indicate coseismic constant slip regions starting from 20 cm to the maximum value, stepping every 20 cm. (a) and (b) show horizontal and vertical cumulative displacements, respectively, inverting with $R = 1$ and $\gamma = 2.5\,\mathrm{cm}^{-1}$. (c) and (d) show horizontal and vertical cumulative displacements, respectively, inverting with $R = 15$ and $\gamma = 2.5\,\mathrm{cm}^{-1}$. (e) and (f) show horizontal and vertical cumulative displacements, respectively, for a rake fixed to -90° and a γ value of $25\,\mathrm{cm}^{-1}$. (b) and (d) also show the rake of those patches which are characterized by a slip value larger than 20 per cent of the maximum slip value. The slip and the displacements are computed as the value of the last day of our analysis (namely, the 306 d after the mainshock) less the value of the first day after the mainshock.

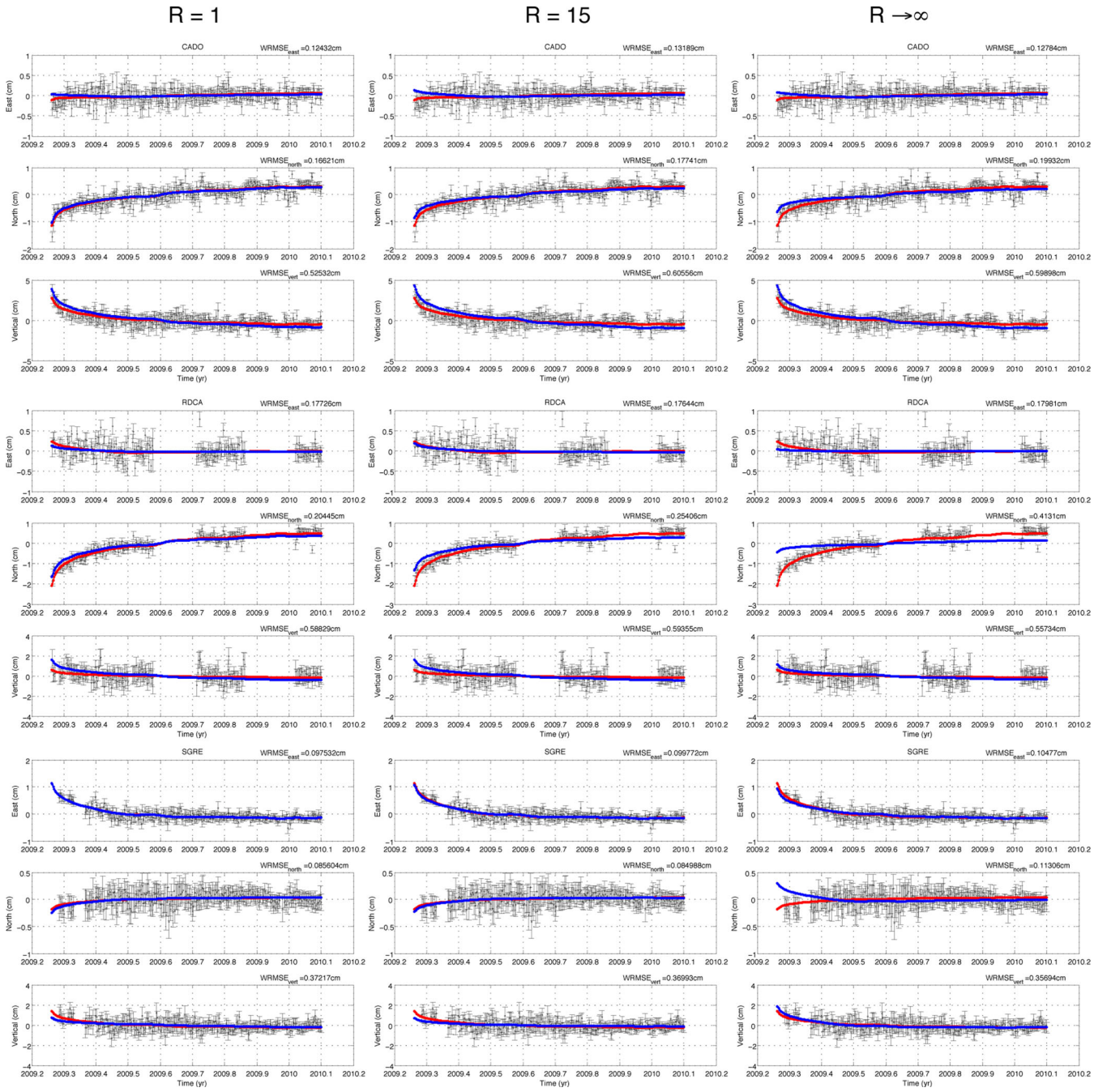

Figure 7. Post-seismic time series for the stations CADO, RDCA and SGRE. Black circles are the original data and black bars are the corresponding one-sigma uncertainties. Red lines represent the time-series decomposition. From right to left, blue lines are the modelled time-series for a rake angle fixed to –90° ($R \rightarrow \infty$), slightly variable ($R = 15$) and completely variable ($R = 1$).

Introducing the Campotosto fault, the fault plane region that undergoes afterslip is the same in all our inversions and is named region C (Fig. 9). Thus, for all the calculation of the next section, we take into account patches that belong to regions A of the Paganica fault and C of the Campotosto fault.

7 DETERMINATION OF FAULTS FRICTIONAL PROPERTIES

From laboratory experiments (e.g. Dietrich 1979; Ruina 1983), it is well known that the friction coefficient (μ) between two blocks of rock varies with the relative velocity between them (V) and one or more state parameters (θ_1, θ_2, ...), which are representative of the state of the sliding surface. The Dieterich–Ruina rate- and state-dependent friction formulation is:

$$\mu(V, \theta) = \mu^* + a \ln \frac{V}{V^*} + b \ln \frac{V^* \theta}{D_c}, \quad (1)$$

$$\dot{\theta} = 1 - \frac{V\theta}{D_c}, \quad (2)$$

where μ^* is the nominal coefficient of friction at the steady reference velocity, V^* is a reference velocity, D_c is the so-called critical

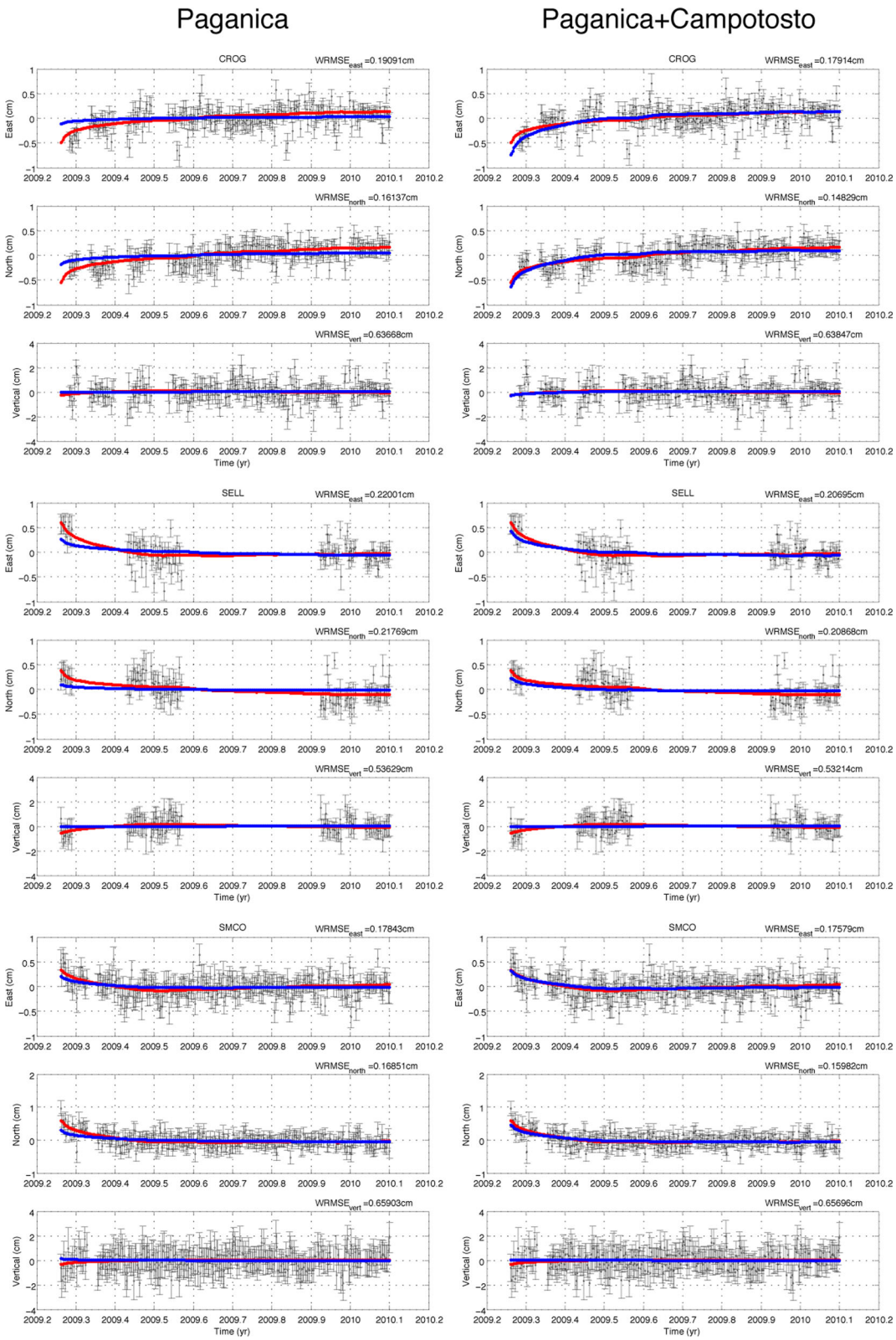

Figure 8. Post-seismic time-series of the stations CROG, SELL and SMCO. Colours are the same of Fig. 7. On the left, the time-series used to invert for afterslip only on the Paganica fault (P2) are shown; on the right, we present the results obtained considering also the Campotosto fault (C1). It is worth noting that a better fit is remarkable for the very first days, especially for the horizontal components.

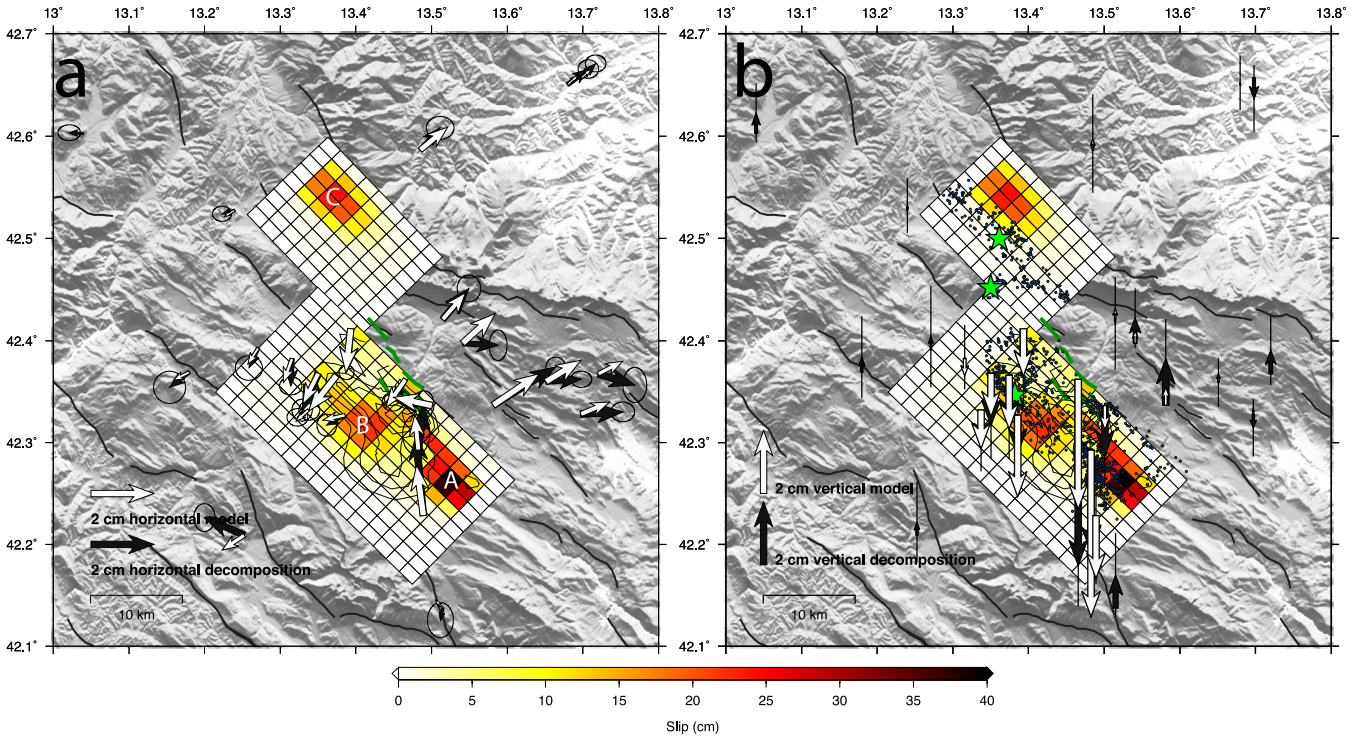

Figure 9. Post-seismic slip model allowing slip on both Paganica (P2) and Campotosto (C1) faults. Contouring lines indicate coseismic constant slip regions starting from 20 cm to the maximum value, stepping every 20 cm. (a) and (b) show horizontal and vertical cumulative displacements, respectively, for the near-field stations. γ and R values are 2.5 cm^{-1} and 15 for the Paganica fault and 2 cm^{-1} and 15 for the Campotosto fault. Capital letters A, B and C indicate the afterslip regions. Green stars show the location of the mainshock (on the Paganica fault) and the two aftershocks of April 9 and June 22. The slip and the displacements are computed as the value of the last day of our analysis (namely, the 306 day after the mainshock) less the value of the first day after the mainshock. Blue dots in (b) are the aftershocks from Chiaraluce *et al.* (2011).

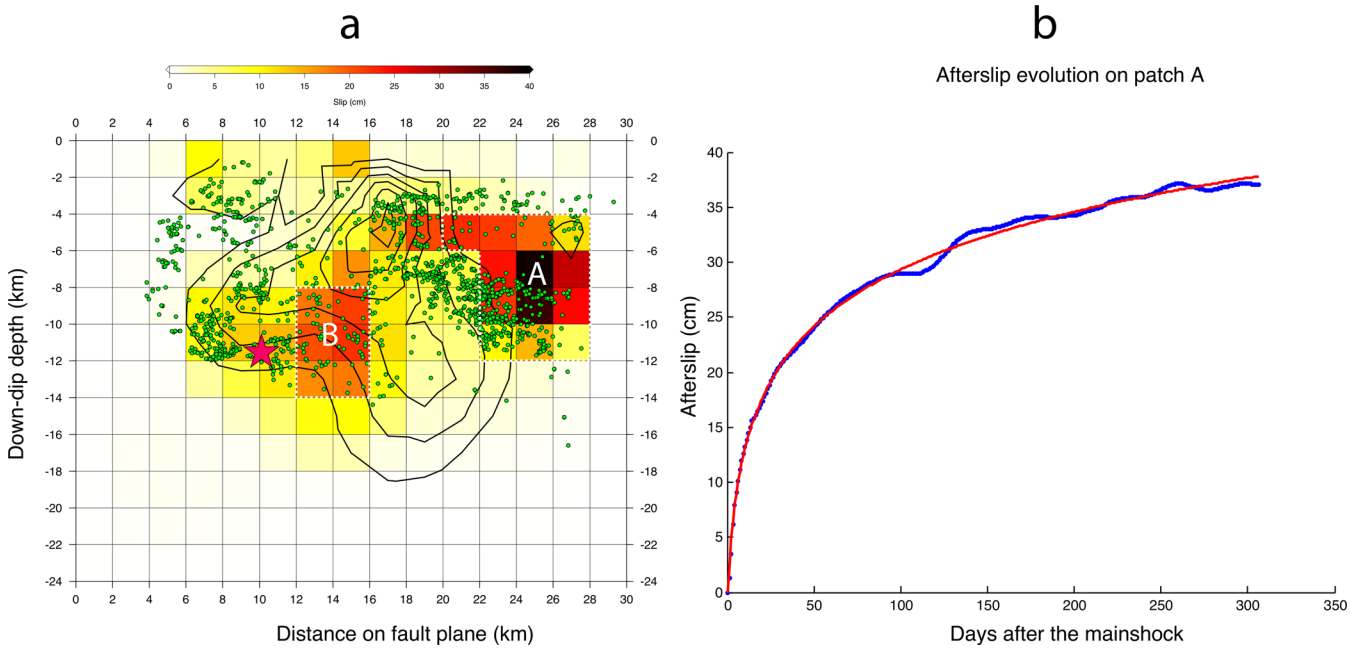

Figure 10. (a) Afterslip distribution on the Paganica fault plane (P2) when both Paganica and Campotosto faults are taken into account in the inversion. Green dots are the projected aftershocks used to deduce the fault and derived from Chiaraluce *et al.* (2011) (see Section 2). Contour lines represent the coseismic slip, as in previous figures. The purple star localizes the mainshock event. Capital letters A and B indicate the main afterslip regions. Region A is used for the calculation of the frictional parameter $a - b$. (b) Afterslip history of the main afterslip patch experiencing coseismic stress increase. The blue dots represent the afterslip deduced from the inversion of GPS data. The red line represents the frictional model expressed by the formula (3). The parameter values are: $\alpha \sim 7.7$ cm, $\beta \sim 4.3$ cm d^{-1} and have been obtained through an unconstrained non-linear minimization of the sum of squared residuals.

slip distance, a and b are both positive constants. If $b > a$ ($a > b$), the constitutive equations predict long-term velocity-weakening (velocity-strengthening) effects on friction. In this section, we estimate the frictional parameter $a - b$ on selected regions of the two faults activated during the sequence, by comparing the temporal evolution of slip $\delta(t)$ with the predictions of a 0-dimensional model (i.e. a spring slider) of a velocity-strengthening fault. In particular, within the afterlip regions A and C (specified in Section 6), we estimate $a - b$ on those patches where the mainshock caused a positive variation of Coulomb stress (ΔCFF). The ΔCFF is calculated using the coseismic slip distribution described in Section 6, a rigidity value of 30 GPa and a Poisson ratio of 0.25. The shear stress is evaluated along the slip direction of each patch. We obtain ΔCFF values in the range 0.3–2.1 MPa for region A. The whole region C on the Campotosto fault is loaded by a ΔCFF$\sim$0.03 MPa, induced by the coseismic slip on the Paganica fault.

For times larger than the first epoch recorded after the mainshock (t_1), the following model can be used (see Appendix A for more details on its derivation):

$$\delta(t) - \delta(t_1) \approx \alpha \ln\left[\frac{\alpha + \beta t}{\alpha + \beta t_1}\right] \text{ for } t_1 \leq t \ll t_d = \frac{\alpha}{V_{pl}}, \tag{3}$$

where, as in Marone *et al.* (1991), $\alpha = (a - b)\sigma/k = V_{\rm pl}t_{\rm d}$ is a characteristic slip and $\beta = V_+$ is the starting sliding velocity on the patch at the beginning of the post-seismic phase ($t \approx 0$). k is the stiffness of the spring in the fault analogue model, σ is the effective normal stress, $V_{\rm pl}$ is the loading plate velocity and $t_{\rm d}$ is a characteristic decay time. From this expression, we can estimate the two parameters α and β by comparison with the inverted slip histories. To ensure the validity of relation (3), we need to verify if the time spanned in our analysis (306 d) is much smaller than the characteristic time $t_{\rm d} = \alpha/V_{\rm pl}$. The Paganica fault slip-rate is estimated to be in the range of 0.2–0.7 mm yr^{-1} from geological data (Boncio *et al.* 2010; Cinti *et al.* 2011). On the other hand, D'Agostino *et al.* (2011) showed that interseismic strain loading on a single fault system, with a slip rate of $\sim$3 mm yr^{-1}, is able to reproduce the main features of the observed GPS velocity field across this sector of the Apennines. Considering a range of values for $V_{\rm pl}$ of 0.2–3 mm yr^{-1}, we obtain that the minimum decay time is $t_{\rm d} \sim 2.8$ yr, which is significantly bigger than the observation time span. Consequently, the relation (3) is valid and we can use the estimation of the parameter β, which varies between 0.3 and 4.3 cm d^{-1} on the selected patches, to estimate the $a - b$ frictional parameter. Indeed, the following relation is valid for a velocity-strengthening region (Perfettini & Ampuero 2008):

$$\Delta\text{CFF} = (a - b)\sigma \log\frac{\beta}{V_{pl}} \quad \text{for} \quad \Delta\text{CFF} > 0, \tag{4}$$

where σ is the effective normal stress on the patch, which we evaluate as: $\sigma = p_{\rm lit}(z) - p_{\rm W}(z) - \Delta p(z)$, where $p_{\rm lit}$ and $p_{\rm W}$ are the lithostatic and the hydrostatic pressure, respectively, Δp is the pore overpressure and z is the patch depth. In order to evaluate the lithostatic pressure, we use a density profile of 2600 kg m^{-3} above 4 km depth and 2800 kg m^{-3} below it, as in Trasatti *et al.* (2011). We assume the Δp estimate given by Terakawa *et al.* (2010) for the L'Aquila (2009) earthquake, obtaining σ values in the range $\sim$40–100 MPa. The frictional parameter $a - b$ varies in the range 10^{-4}–10^{-3}, and, assuming the two end-members $V_{\rm pl}$ values, 0.2 and 3 mm yr^{-1}, we find a value around 10^{-3} in $\sim$80 per cent of the selected patches.

8 DISCUSSION

We analyse GPS displacement time-series with a method that allows the data to reveal the temporal and spatial evolution of crustal deformation during the 2009 L'Aquila seismic sequence. This is important in the study of both coseismic and post-seismic deformation. Coseismic displacements, in fact, can be significantly biased by the presence of a fast initial post-seismic transient. This is particularly critical for GPS stations missing data for some time interval after the mainshock (e.g. survey-mode GPS stations reoccupied later after the mainshock). In order to minimize this potential systematic error, which in general tends to provide overestimated jumps, a possibility is to estimate the decay time of a time-dependent deformation model from the continuous GPS stations, adopting a logarithmic or exponential model, under the assumption that it is the same for the entire network (e.g. Devoti *et al.* 2012). Unlike that approach, here we use the PCAIM method to estimate a good approximation of the initial post-seismic signal in the presence of missing data, while consistently estimating the coseismic displacements. A drawback of the method adopted in this work is that the fit to the post-seismic displacement time-series is not always the best one, since assuming a logarithmic or exponential function the amplitude and time-decay constant of the relaxation process can be optimized for each observed time-series (e.g. Devoti *et al.* 2012). However, *a priori* assumptions on the temporal evolution of the post-seismic deformation can bias the conclusions or prevent the identification of superimposed transients on the relaxation process.

The decomposed post-seismic signal can be compared with the two laws commonly used to fit the temporal dependence in the post-seismic displacements (i.e. exponential or logarithmic). As shown in Fig. 3(c), for the exponential case we find a decay constant of 31.2 d, which is in agreement with values obtained in previous studies (20–40 d by Cheloni *et al.* 2010 and D'Agostino *et al.* 2012; 3.5–70.3 d by Devoti *et al.* 2012). However, a logarithmic function also fits the temporal evolution of the decomposed signal, particularly in its initial faster phase, and we find a decay constant of $\sim$1 d. This finding is important because a logarithmic model is in agreement with a physically based frictional model of post-seismic sliding (as described in Section 7).

Geodetic observations rather well constrain the position and geometry of the Paganica fault (e.g. Cheloni *et al.* 2010; Serpelloni *et al.* 2012), with a modelled plane that well fits the distribution of aftershocks in the northern part of the fault. On the contrary, the geometry of the Campotosto fault can be derived only from the distribution of seismicity, since our analysis does not reveal any superficial displacement related to the largest aftershock occurred on this segment. Although aftershocks highlight a complex geometry of the fault system activated during the sequence, our analysis shows that the available GPS observations do not justify the use of a more complex fault geometry for both the Paganica, particularly in its southern portion, and the Campotosto faults. On the other hand, post-seismic GPS displacements are sensitive to afterslip occurring on the Campotosto fault. Comparing the χ^2 statistics inverting for afterslip only on the Paganica fault and on both the Paganica and Campotosto faults, and using an F-test, we find a significant (at 95 per cent confidence) improvement in the fit. In particular, if we consider the stations close to the Campotosto fault (see Figs 8 and 9), we find that the improvement of the WRMSE is $\sim$10 per cent for the first 2 weeks and $\sim$5 per cent for the whole time spanned. This provides validity to our inference about afterlip on the Campotosto fault. Thus, regardless of the spatial separation between the two structures (e.g. Barnhart & Lohman 2013), the main coseismic

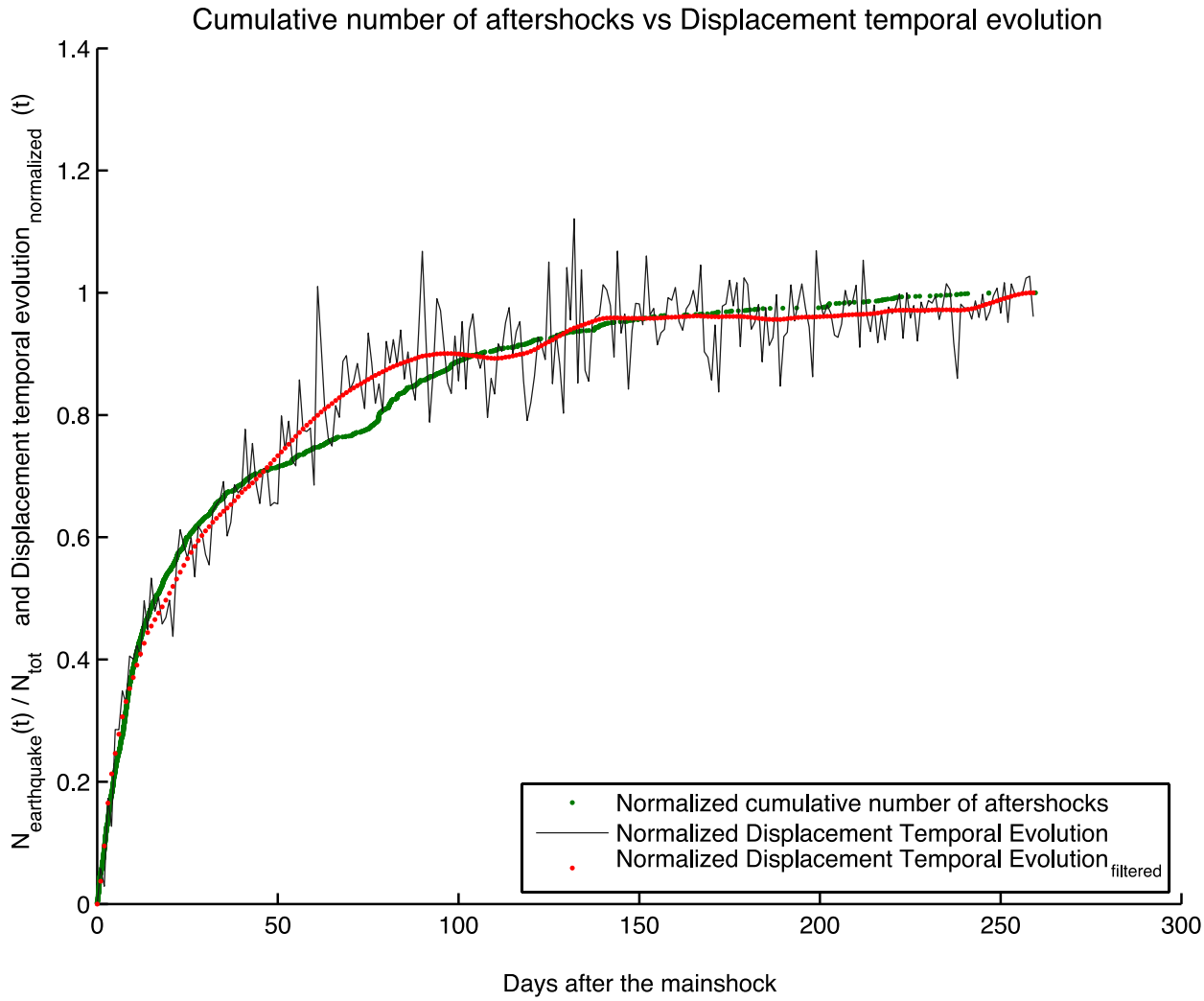

Figure 11. Temporal evolution of GPS post-seismic displacement (red line, as in Fig. 3c) and cumulative number of aftershocks (green line). We can note that at 77 d after the mainshock, in correspondence to the June 22 aftershock, there is a sudden increase of the cumulative number of aftershocks.

rupture on the Paganica fault is likely to have induced afterlip also on the Campotosto fault.

Afterslip on the Paganica fault occurs on portions of the fault located SE and NW respect to the main coseismic slip patch (Figs 6 and 10a), as pointed out also by Cheloni *et al.* (2010) and D'Agostino *et al.* (2012). However, we find that only the SE region (letter A in Figs 9 and 10a) is a stable feature in our post-seismic inversions, whereas the location of the NW afterslip region (letter B in Figs 9 and 10a) is sensitive to the rake constraints adopted, suggesting that a variable rake inversion is worth to be performed before eventually fixing the rake value, as done in previous studies.

Afterslip on the Campotosto fault released (after 306 d from the L'Aquila mainshock) a total amount of equivalent seismic moment of 2.9×10^{17} N·m (for a rigidity value of 30 GPa), and it is shallower and about complementary to the distribution of aftershocks (Fig. 9). Afterslip on the Campotosto fault is likely to have loaded these aftershocks. Indeed, introducing the Campotosto fault and taking into account the afterslip of the first 3 d after the mainshock, the Coulomb stress increase (ΔCFF) in the region of the April 9 aftershock doubles, passing from 0.03 to 0.06 MPa. In particular, we evaluate that afterslip on the Campotosto fault alone induced more than the 98 per cent of the 0.03 MPa increase occurred during the post-seismic stage. The M_w 4.4 aftershock of June 22 (77 d after the mainshock, see Figs 9 and 11), on the Campotosto fault, is located below the region undergoing afterslip. This event occurred in a fault region that was affected by a negligible coseismic stress change due to the L'Aquila mainshock (ΔCFF $<$ 0.01 MPa). Instead, the same fault region experienced a Coulomb stress increase of 0.06 MPa due to afterslip on the Campotosto fault, and it was slightly unloaded by afterslip on the Paganica fault, resulting in a net increase of stress after 77 d of post-seismic stage of 0.05 MPa. These considerations enforce our finding that, following the April 6 mainshock, the Campotosto fault has been activated not only seismically (i.e. aftershocks, e.g. Chiaraluce *et al.* 2011), but also aseismically.

The coseismic slip distribution and the temporal evolution of afterslip are used to constrain the parameters of a frictional model of afterslip, based on the rate- and state-dependent constitutive laws, as described in Section 7. We use the model of Marone *et al.* (1991), which applies to velocity-strengthening fault regions, where $a - b > 0$ is a measure of the long-term increase of friction after a sudden slip rate increase. For fault regions that show a robust afterslip pattern (see Section 6) and positive values of the Coulomb stress change, we estimate the $a - b$ frictional parameter. Since afterslip patches have a stationary location (i.e. creep propagation is not evident) it is not necessary to model the temporal evolution of slip

taking into account elastic interaction between patches (e.g. Wesson 1980). Then, as in Perfettini *et al.* (2010), the model is applied to single patches, neglecting the mutual elastic interaction between them during the post-seismic stage. The estimate of $a-b$ for a given patch is slightly affected by the current uncertainty of the long-term fault slip rate ($V_{\rm pl}$), which is assumed to vary in the range 0.2–3 mm yr^{-1} (see eq. 4). We find $a-b$ values in the range 10^{-4}–10^{-3}, with the most frequent value of the order of 10^{-3}, in agreement with studies of fault rocks typical of these regions at elevated temperatures and under fluid-saturated conditions (Scuderi *et al.* 2013). Small $a-b$ values, such as 10^{-3} (Marone *et al.* 1991), characterize fault regions where transitions between velocity weakening ($a-b<0$) and velocity strengthening ($a-b>0$) occur. These regions may undergo both afterslip and aftershocks during the post-seismic phase (Boatwright & Cocco 1996). Fig. 10(a) shows the distribution of afterslip on the Paganica fault plane superimposed to the aftershock projections on the same plane. We note that the afterslip region A is also characterized by a high concentration of aftershocks, in agreement with our estimates of the $a-b$ parameter. Fig. 10(b) shows the slip temporal evolution and the fit of a spring-slider model for the main afterslip patch of region A considered in the computation of $a-b$.

Fig. 11 shows that the time evolution of afterslip and the cumulated number of aftershocks follow approximately the same decay law. A similar correlation has been observed by Perfettini & Avouac (2007) for the 1992 Landers earthquake. According to Helmstetter & Shaw (2009), the similar time decay and duration of afterslip and aftershocks suggests that afterslip may influence the aftershock productivity, even if afterslip is not the sole mechanism of aftershock triggering. In particular, the seismicity rate can be affected by both the stress step induced by coseismic slip and the stressing rate induced by afterslip. Lolli *et al.* (2011) showed that the rate of aftershocks of the L'Aquila sequence decays less fast than Omori law in the first 80 d, during which the Omori exponent p increased from 0.5 to 1.2. Using a rate- and state-dependent law, the seismicity rate produced by a coseismic stress change decays with $p=1$, while time-dependent values of p suggest that also afterslip affects the seismicity rate, causing mainly unloading of the potential sources of aftershocks (Helmstetter & Shaw 2009). This is in agreement with the fact that many aftershocks occur on fault patches undergoing afterslip (see Fig. 10a), thus, on average, experiencing unloading due to afterslip (under the hypothesis of a focal mechanism similar to the mainshock one).

Fig. 11 shows a transient signal characterized by a flattening followed by an increase of displacements as a function of time at ∼130 d after the April 6 mainshock. D'Agostino *et al.* (2012) found a transient in InSAR displacement time-series about in the same period of time, and ascribed this signal to atmospheric errors in the estimation of InSAR time-series, since they did not find a similar signature in the GPS time-series. Unlike D'Agostino *et al.* (2012), where the assumption of an exponential function is made to reproduce the GPS displacements, in our analysis the transient is retrieved as a signal recorded by the whole GPS network. The fact that this transient signal is common to two different data sets favours the hypothesis that it is not an artefact due to some acquisition problem. This signal can be due to a change in sign of the footwall displacements near the Paganica fault, as InSAR observations show at about 120 d after the mainshock (see fig. 9 of D'Agostino *et al.* 2012). It is not to be excluded that the detected signal can be due to a poroelastic effect. Indeed, on the footwall of the Paganica fault, our estimation of poroelastic rebound effects on surface displacements predicts opposite values with respect to the observed cumulative ones. In particular, while data indicate uplift, the modelled poroelastic effect indicates subsidence. Anyway, a more detailed and quantitative analysis is required to better understand the causes of this signal, which is beyond the scope of this work.

9 CONCLUSIONS

We determined the coseismic and post-seismic slip distributions related to the 2009 L'Aquila earthquake sequence applying PCAIM to GPS displacement time-series. We found that this approach, which had been previously used to study larger magnitude earthquakes (i.e. with greater displacements), applies also to moderate magnitude earthquakes, and turns out to be particularly efficient to estimate the coseismic displacements minimizing the potential systematic bias due to unknown post-seismic evolution. The approach used allowed us to recover transient signals that could be superimposed to the main post-seismic relaxation process, since it does not prescribe a temporal evolution of the observed displacements that could filter out those signals.

We proposed a method to determine fault geometries based on the distribution of relocated aftershocks, but we also showed that geometric complexities of the main sources involved in the sequence are unnecessary to explain the observed GPS displacements. We found that both the coseismic and post-seismic slip distributions are sensitive to *a priori* constraints on the rake variability, and conclude that GPS observations are well reproduced by a variable rake-slip distribution on simple planar faults. The coseismic and post-seismic slip distributions obtained for the Paganica fault are in agreement with previous studies from GPS data, but we found that GPS displacements recorded the occurrence of post-seismic afterslip also on the Campotosto fault, where one of the two largest aftershocks of the L'Aquila sequence nucleated on April 9. Our results suggest that, in order to correctly explain and interpret the L'Aquila (2009) seismic sequence, it is important to take into account all the structures that show clues of post-seismic activity, such as aftershock production.

We provided clues about the frictional properties for normal faults in the Apennines from field geodetic observations. In particular, we estimated the frictional parameters of velocity-strengthening regions of the fault planes that undergo afterslip, while experiencing a positive coseismic variation of Coulomb stress. The $a-b$ values obtained suggest that afterslip developed in transition regions between a velocity-weakening behaviour and a velocity-strengthening one. We conclude that the afterslip regions on the Paganica fault mitigated the occurrence of aftershocks. Instead, the afterslip developed on the Campotosto fault brought closer to failure the sources of aftershocks occurred in that region.

ACKNOWLEDGEMENTS

We thank Andrew Kositsky, Nina Lin and Jean-Philippe Avouac for the helpful discussions about the PCAIM code. We thank the Unità Funzionale 'Analisi Dati per la Geodesia', of the INGV Centro Nazionale Terremoti, for making available GPS data from the CaGeoNet network and all institutions that made available continuous GPS data in the epicentral area, particularly the INGV-RING team, the Italian Space Agency (ASI), Leica Geosystem, Geotop and the Laboratori Nazionali del Gran Sasso (INFN). We thank Lauro Chiaraluce for constructive discussions about the relocated catalogues of aftershocks, and Antonio Avallone for comments and suggestions. Comments from the Editor (Dancan Agnew) and two anonymous

reviewers significantly improved the quality of the manuscript. Some of the figures have been created using the Generic Mapping Tools (GMT) software (Wessel & Smith 1998). The computation of the ΔCFF has been performed using the Coulomb 3.3 software (Toda *et al.* 2011).

REFERENCES

Anzidei, M. *et al.*, 2009. Coseismic deformation of the destructive April 6, 2009 L'Aquila earthquake (central Italy) from GPS data, *Geophys. Res. Lett.,* **36,** L17307, doi:10.1029/2009GL039145.

Atzori, S. *et al.*, 2009. Finite fault inversion of DInSAR coseismic displacement of the 2009 L'Aquila earthquake (central Italy), *Geophys. Res. Lett.,* **36,** L15305, doi:10.1029/ 2009GL039293.

Barbot, S. & Fialko, Y., 2010. A unified continuum representation of post-seismic relaxation mechanisms: semi-analytic models of afterslip, poroelastic rebound and viscoelastic flow, *Geophys. J. Int.,* **182,** 1124–1140.

Barchi, M., Galadini, F., Lavecchia, G., Messina, P., Michetti, A.M., Peruzza, L., Pizzi, A. & Tondi, E., 2000. Sintesi delle conoscenze sulle faglie attive in Italia Centrale: parametrizzazione ai fini della caratterizzazione della pericolosità sismica, CNR-Gruppo Nazionale per la Difesa dai Terremoti, Roma, pp. 62.

Barnhart, W.D. & Lohman, R.B., 2013. Phantom earthquakes and triggered aseismic creep: vertical partitioning of strain during earthquake sequences in Iran, *Geophys. Res. Lett.,* **40,** 819–823.

Belardinelli, M.E., Cocco, M., Coutant, O. & Cotton, F., 1999. Redistribution of dynamic stress during coseismic ruptures: evidence for fault interaction and earthquake triggering, *J. geophys. Res.,* **104**(B7), 14 925–14 945.

Boatwright, J. & Cocco, M., 1996. Frictional constraints on crustal faulting, *J. geophys. Res.,* **101**(B6), 13 895–13 909.

Boncio, P., Lavecchia, G. & Pace, B., 2004. Defining a model of 3D seismogenic sources for seismic hazard assessment applications: the case of Central Apennines (Italy), *J. Seismol.,* **8,** 407–425.

Boncio, P., Pizzi, A., Brozzetti, F., Pomposo, G., Lavecchia, G., Di Naccio, D. & Ferrarini, F., 2010. Coseismic ground deformation of the 6 April 2009 L'Aquila earthquake (central Italy, M_w6.3). *Geophys. Res. Lett.,* **37,** L06308, doi:10.1029/2010GL042807.

Cheloni, D. *et al.*, 2010. Coseismic and initial post-seismic slip of the 2009 M_W 6.3 L'Aquila earthquake, Italy, from GPS measurements, *Geophys. J. Int.,* **181,** 1539–1546.

Chiarabba, C. *et al.*, 2009. The 2009 L'Aquila (central Italy) M_w 6.3 earthquake: mainshock and aftershocks, *Geophys. Res. Lett.,* **36,** L18308, doi:10.1029/2009GL039627.

Chiaraluce, L., Valoroso, L., Piccinini, D., Di Stefano, R. & De Gori, P., 2011. The anatomy of the 2009 L'Aquila normal fault system (central Italy) imaged by high resolution foreshock and aftershock locations, *J. geophys. Res.,* **116,** B12311, doi:10.1029/2011JB008352.

Cinti, F.R. *et al.*, 2011. Evidence for surface faulting events along the Paganica fault prior to the 6 April 2009 L'Aquila earthquake (central Italy), *J. geophys. Res.,* **116,** B077308, doi:10.1029/2010JB007988.

Cirella, A., Piatanesi, A., Cocco, M., Tinti, E., Scognamiglio, L., Michelini, A., Lomax, A. & Boschi, E., 2009. Rupture history of the 2009 L'Aquila earthquake from non-linear inversion of strong motion and GPS data, *Geophys. Res. Lett.,* **36,** L19304, doi:10.1029/2009GL039795.

D'Agostino, N., Cheloni, D., Fornaro, G., Giuliani, R. & Reale, D., 2012. Space-time distribution of afterslip following the 2009 L'Aquila earthquake, *J. geophys. Res.,* **117,** B02402, doi:10.1029/2011JB008523.

D'Agostino, N., Mantenuto, S., D'Anastasio, E., Giuliani, R., Mattone, M., Calcaterra, S., Gambino, P. & Bonci, L., 2011. Evidence for localized active extension in the central Apennines (Italy) from global positioning system observations, *Geology,* **39,** 291–294.

Devoti, R. *et al.*, 2012. The coseismic and postseismic deformation of the L'Aquila, 2009 earthquake from repeated GPS measurements. *Ital. J. Geosci. (Boll. Soc. Geol. It.),* **131**(3), 348–358.

Dietrich, J.H., 1979. Modeling of fault friction: 1. Experimental results and constitutive equations, *J. geophys. Res.,* **84**(B5), 2161–2168.

Dong, D., Fang, P., Bock, Y., Webb, F., Prawirodirdjo, L., Kedar, S. & Jamason, P., 2006. Spatiotemporal filtering using principal component analysis and Karhunen-Loeve expansion approaches for regional GPS network analysis, *J. geophys. Res.,* **111,** B03405, doi:10.1029/2005JB003806.

Du, B.Y., Aydin, A. & Segall, P., 1992. Comparison of various inversion techniques as applied to the determination of a geophysical deformation model for the 1983 Borah Peak earthquake, *Bull. seism. Soc. Am.,* **82**(4), 1840–1866.

Faure Walker, J.P., Roberts, G.P., Sammonds, P.R. & Cowie, P., 2010. Comparison of earthquake strains over 10^2 and 10^4 year timescales: insights into variability in the seismic cycle in the central Apennines, Italy, *J. geophys. Res.,* **115,** B10, doi:10.1029/2009JB006462.

Fielding, E.J., Lundgren, P.R., Burgmann, R. & Funning, G.J., 2009. Shallow fault-zone dilatancy recovery after the 2003 Bam earthquake in Iran. *Nature,* **458,** doi:10.1038/nature07817.

Fukuda, J., Johnson, K.M., Larson, K.M. & Miyazaki, S., 2009. Fault friction parameters inferred from the early stages of afterslip following the 2003 Tokachi-oki earthquake. *J. geophys. Res.,* **114**(B4), doi:10.1029/2008JB006166.

Galadini, F. & Galli, P., 2000. Active tectonics in the central Apennines (Italy)—input data for seismic hazard assessment, *Nat. Hazards,* **22,** 225–270.

Galli, P., Galadini, F. & Pantosti, D., 2008. Twenty years of paleoseismology in Italy, *Eart. Sci. Rev.,* **88,** 89–117.

Galvani, A., Anzidei, M., Devoti, R., Esposito, A., Pietrantonio, G., Pisani, A. R., Riguzzi, F. & Serpelloni, E., 2013. The interseismic velocity field of the Central Apennine from a dense GPS network, *Annals of Geophysics,* **55,** 5, doi: 10.4401/ag-5634.

Helmstetter, A. & Shaw, B.E., 2009. Afterslip and aftershocks in the rate-and-state friction law, *J. geophys. Res.,* **114,** B01308, doi:10.1029/2007JB005077.

Herrmann, R.B., Malagnini, L. & Munafò, I., 2011. Regional moment tensors of the 2009 L'Aquila earthquake sequence. *Bull. seism. Soc. Am.,* **101,** 975–993.

Hetland, E.A., Musé, P., Simons, M., Lin, Y.N., Agram, P.S. & DiCaprio, C.J., 2012. Multiscale InSAR time series (MInTS) analysis of surface deformation, *J. geophys. Res.,* **117,** B2, doi:10.1029/2011JB008731.

Hsu, Y.J. *et al.*, 2006. Frictional afterslip following the 2005 Nias-Simeulue earthquake, Sumatra, *Science,* **312**(5782), 1921–1926.

Hsu, Y.-J., Segall, P., Yu, S.-B., Kuo, L.-C. & Williams, C.A., 2007. Temporal and spatial variations of post-seismic deformation following the 1999 Chi-Chi, Taiwan earthquake, *Geophys. J. Int.,* **169**(2), 367–379.

Johnson, K.M., Bürgmann, R. & Larson, K., 2006. Frictional properties on the San Andreas Fault near Parkfield, California, inferred from models of afterslip following the 2004 earthquake, *Bull. seism. Soc. Am.,* **96**(4B), S321–S338.

Kositsky, A.P. & Avouac, J.P., 2010. Inverting geodetic time series with a principal component analysis-based inversion method, *J. geophys. Res.,* **115,** B03401, doi:10.1029/2009JB006535.

Lanari, R. *et al.*, 2010. Surface displacements associated with the L'Aquila 2009 M_w 6.3 earthquake (central Italy): new evidences from SBAS-DInSAR time series analysis, *Geophys. Res. Lett.,* **37,** 20, doi:10.1029/2010GL044780.

Langbein, J., 2008. Noise in GPS displacement measurements from Southern California and Southern Nevada, *J. geophys. Res.,* **113**(B5), doi:10.1029/2007JB005247.

Lolli, B., Gasperini, P. & Boschi, E., 2011. Time variations of aftershock decay parameters of the 2009 April 6 L'Aquila (central Italy) earthquake: evidence of the emergence of a negative exponential regime superimposed to the power law. *Geophys. J. Int.,* **185**(2), 764–774.

Marone, C., Scholz, C.H. & Bilham, R., 1991. On the mechanics of earthquake afterslip, *J. geophys. Res.,* **96,** 8441–8452.

Márquez-Azúa, B. & DeMets, C., 2003. Crustal velocity field of Mexico from continuous GPS measurements, 1993 to June 2001: implications for the neotectonics of Mexico, *J. geophys. Res.,* **108,** B9, doi:10.1029/2002JB002241.

Okada, Y., 1985. Surface deformation to shear and tensile faults in a half-space, *Bull. seism. Soc. Am.,* **75,** 1135–1154.

Perfettini, H. & Ampuero, J.P., 2008. Dynamics of a velocity strengthening region: implications for slow earthquakes and postseismic slip, *J. geophys. Res.,* **113**(B9), B09411, doi:10.1029/2007JB005398.
Perfettini, H. & Avouac, J.P., 2007. Modeling afterslip and aftershocks following the 1992 Landers earthquake, *J. geophys. Res.,* **112,** B07409, doi:10.1029/2006JB004399.
Perfettini, H. *et al.*, 2010. Seismic and aseismic slip on the Central Peru megathrust, *Nat. Lett.,* **465,** doi:10.1038/nature09062.
Pollitz, F., Banerjee, P., Grijalva, K., Nagarajan, B. & Bürgmann, R., 2008. Effect of 3-D viscoelastic structure on post-seismic relaxation from the 2004 $M = 9.2$ Sumatra earthquake, *Geophys. J. Int.,* **173,** 189–204.
Pondrelli, S., Salimbeni, S., Morelli, A., Ekstrom, G., Olivieri, M. & Boschi, E., 2010. Seismic moment tensors of the April 2009, L'Aquila (Central Italy), earthquake sequence, *Geophys. J. Int.,* **180,** 238–242.
Rice, J.R. & Gu, J.C., 1983. Earthquake aftereffects and triggered seismic phenomena, *Pure Apll. Geophys.,* **121**(2), 187–219.
Ruina, A., 1983. Slip instability and state variable friction laws, *J. geophys. Res.,* **88**(B12), 10 359–10 370.
Scognamiglio, L., Tinti, E., Michelini, A., Dreger, D., Cirella, A., Cocco, M., Mazza, S. & Piatanesi, A., 2010. Fast determination of moment tensors and rupture history: what has been learned from the 6 April 2009 L'Aquila earthquake sequence, *Seismol. Res. Lett.,* **81**(6), 892–906.
Scuderi, M.M., Niemeijer, A.R., Collettini, C. & Marone, C., 2013. Frictional properties and slip stability of active faults within carbonate–evaporite sequences. The role of dolomite and anhydrite, *Earth planet. Sci. Lett.,* **369–370,** 220–232.
Serpelloni, E., Anderlini, L. & Belardinelli, M.E., 2012. Fault geometry, coseismic-slip distribution and Coulomb stress change associated with the 2009 April 6, M_W 6.3, L'Aquila earthquake from inversion of GPS displacements, *Geophys. J. Int.,* **188,** 473–489.
Serpelloni, E., Anzidei, M., Baldi, P., Casula, G. & Galvani, A., 2006. GPS measurement of active strains across the Apennines, *Ann. Geophys.,* **49,** 319–329.
Serpelloni, E., Faccenna, C., Spada, G., Dong, D. & Williams, S.D.P., 2013. Vertical GPS ground motion rates in the Euro-Mediterranean region: new evidence of velocity gradients at different spatial scales along the Nubia-Eurasia plate boundary, *J. geophys. Res.,* **118,** doi:10.1002/2013JB010102.
Suito, H. & Freymueller, J.T., 2009. A viscoelastic and afterslip postseismic deformation model for the 1964 Alaska earthquake, *J. geophys. Res.,* **114,** B11404, doi:10.1029/2008JB005954.
Terakawa, T., Zoporowski, A., Galvan, B. & Miller, S.A., 2010. High-pressure fluid at hypocentral depths in the L'Aquila region inferred from earthquake focal mechanisms, *Geology,* **38**(11), 995–998.
Toda, S., Stein, R., Sevilgen, V. & Lin, J., 2011. Coulomb 3.3 Graphic-rich deformation and stress-change software for earthquake, tectonic, and volcano research and teaching—user guide: U.S. Geological Survey Open-File Report 2011–1060, 63 p. Available at: http://earthquake.usgs.gov/research/modeling/coulomb/download/Coulomb31_UserGuide.pdf (last accessed 1 November 2013).
Trasatti, E., Kyriakopoulos, C. & Chini, M., 2011. Finite element inversion of DInSAR data from the Mw 6.3 L'Aquila earthquake, 2009 (Italy), *Geophys. Res. Lett.,* **38,** doi:10.1029/2011GL046714.
Valensise, G. & Pantosti, D., 2001. The investigation of potential earthquake sources in peninsular Italy: a review, *J. Seismol.,* **5,** 287–306.
Valoroso, L., Chiaraluce, L., Piccinini, D., Di Stefano, R., Schaff, D. & Waldhauser, F., 2013. Radiography of a normal fault system by 64,000 high-precision earthquake locations: the 2009 L'Aquila (central Italy) case study, *J. geophys. Res.,* **118,** doi:10.1002/jgrb.50130.
Viti, M., Mantovani, E., Cenni, N. & Vannucchi, A., 2012. Post-seismic relaxation: an example of earthquake triggering in the Apennine belt (1915–1920), *J. Geodyn.,* **61,** 57–67.
Walters, R.J. *et al.*, 2009. The 2009 L'Aquila earthquake (central Italy): a source mechanism and implications for seismic hazard, *Geophys. Res. Lett.,* **36,** L17312, doi:10.1029/2009GL039337.
Wdowinski, S., Bock, Y., Zhang, J., Fang, P. & Genrich, J., 1997. Southern California permanent GPS geodetic array: spatial filtering of daily positions for estimating coseismic and postseismic displacements induced by the 1992 Landers earthquake, *J. Geophys. Res.,* **102,** 18 057–18070.
Wessel, P. & Smith, W.H.F., 1998. New, improved version of the generic mapping tools released, EOS, Trans, *Am. geophys. Un.,* **79,** 579, doi:10.1029/98EO00426.
Wesson, R., 1980. *Letter to Fournier d'Albe, 17 April 1980,* USGS.
Williams, S.D.P., 2003. Offsets in global positioning system time series. *J. geophys. Res.,* **108,** B6, doi:10.1029/2002JB002156.

APPENDIX A: SLIP MODEL

A1: Slip evolution

Let us define t_0 as the origin time of the mainshock, and let us assume that $t_0 = 0$ s. Let us call stress rise time the time necessary to a patch to reach the static final value of stress, and slip rise time the time necessary to a patch to slip coseismically. Let us consider a fault patch that undergoes an increase of stress of duration t_r. In first approximation, we can say that the stress rise time t_r is equal to the sum of the slip rise time and the time necessary to the rupture to reach the patch under study. From Cirella *et al.* (2009), we deduce a range of values for the stress time rise of the L'Aquila (2009) earthquake of 1–10 s, that is of the same magnitude of the time necessary to reach a static stress level for different earthquakes (e.g. ∼14 s for the Irpinia 1980, earthquake, see Belardinelli *et al.* 1999).

The actual slip evolution $\delta(t)$ can be obtained as the sum of the coseismic (δ_{cs}) and post-seismic (δ_{as}) slip distributions, where $\delta_{\rm as}(t)$ is the afterslip developed for $t \geq t_r$. The PCAIM method adopted allows us to recover the spatiotemporal evolution of slip on the fault. Indeed, we find, from the inversion of the spatial part, the principal slip components $L_{\rm p\times r}$ and we know from the decomposition the matrix $S_{\rm r\times r}{V_{\rm r\times n}}^{\rm T}$ (see Section S2.1). Consequently, we can calculate the matrix $LSV^{\rm T}$, which contains the slip evolution of each patch $\delta^{\rm dat}(t)$. This quantity can be written as the sum of the coseismic and afterslip slip distributions of Section 6: $\delta^{\rm dat}(t) = {\delta_{cs}}^{\rm dat} + {\delta_{as}}^{\rm dat}(t)$. The quantity ${\delta_{cs}}^{\rm dat}$ is calculated for $t = t_1$, that is for the first day after the mainshock, and we are not able to resolve it for smaller times. At the same time ${\delta_{as}}^{\rm dat}(t)$ is the slip increment developed after the first day, as retrieved from our data. Assuming that the slip evolution derived inverting data corresponds to the actual slip, we can write:

$$\delta_{cs}^{\rm dat} + \delta_{as}^{\rm dat}(t) = \delta^{\rm dat}(t) = \delta(t) = \delta_{cs} + \delta_{as}(t) \text{ for } t \geq t_1, \quad \text{(A1)}$$

and since ${\delta_{as}}^{\rm dat}(t_1) = 0$, the value ${\delta_{cs}}^{\rm dat}$ is given by:

$$\delta_{cs}^{\rm dat} = \delta^{\rm dat}(t_1) = \delta(t_1) = \delta_{cs} + \delta_{as}(t_1). \quad \text{(A2)}$$

A2: Afterslip model

Adopting a rate- and state-dependent frictional sliding law (eqs 1 and 2 of the main text), and considering a velocity-strengthening patch in a steady-state approximation, we can model it with a spring-slider system, and the following relation is valid (Marone *et al.* 1991):

$$\delta(t) \approx m(t) = m_{cs} + m_{as}(t)$$
$$= m_{cs} + \alpha \ln\left[1 + \frac{\beta}{\alpha}(t - t_r)\right] \text{ for } t_r \leq t \ll t_d = \frac{\alpha}{V_{pl}}, \quad \text{(A3)}$$

where $\delta(t)$ is the actual slip occurred on the patch, $m(t)$ is the modelled temporal evolution of slip due to the stress increase, which

is composed by a modelled coseismic slip m_{cs} at $t = t_r$ and a modelled afterslip $m_{as}(t)$. In particular, as in Marone *et al.* (1991), $\alpha = (a - b)\sigma/k = V_{pl}t_d$ is a characteristic slip and $\beta = V_+$ is the starting sliding velocity on the patch at the beginning of the post-seismic phase ($t \approx 0$). k is the stiffness of the spring in the fault analogue model, σ is the effective normal stress on the patch, V_{pl} is the loading plate velocity and t_d is a characteristic decay time. m_{cs} is a short-term slip undergone by the velocity-strengthening patch, that is, it is the slip that occurs during the application of the stress perturbation ($t_0 < t \leq t_r$, where t_0 is the origin time of the mainshock, which has been assumed equal to 0 s). A short-term slip was predicted by Marone *et al.* (1991) and indicated with the notation $U_C{}^S$. To compare the model $m(t)$ with the slip distributions at our disposal, deduced from daily sampled data, we have to find a model for the afterslip that is valid for times $t \geq t_1$, that is for times greater than the first day after the mainshock. Considering times greater than t_1, we can rewrite the left side of formula (A3) through the value derived from the measurements:

$$\begin{aligned}\delta_{cs} + \delta_{as}(t) &= \delta_{cs}^{\mathrm{dat}} + \delta_{as}^{\mathrm{dat}}(t) = \delta(t)\\ &\approx m(t) = m_{cs} + m_{as}(t) \text{ for } t_1 \leq t \ll t_d, \end{aligned} \tag{A4}$$

and since $t_r \sim 1$ s $<< t_1 = 0.43$ d $\leq t$, we can neglect it in (A3) and we obtain:

$$\begin{aligned}\delta_{cs}^{\mathrm{dat}} + \delta_{as}^{\mathrm{dat}}(t) &\approx m(t) = m_{cs} + m_{as}(t)\\ &\approx m_{cs} + \alpha \ln\left[1 + \frac{\beta}{\alpha}t\right] \text{ for } t_1 \leq t \ll t_d. \end{aligned} \tag{A5}$$

We seek a model for the afterslip at our disposal, $\delta_{as}{}^{\mathrm{dat}}$, that is valid for times $t \geq t_1$. From eqs (A1)–(A5), we can write:

$$\begin{aligned}\delta_{as}^{\mathrm{dat}}(t) &= \delta_{as}(t) + \delta_{cs} - \delta_{cs}^{\mathrm{dat}} = \delta_{as}(t) + \delta_{cs} - \delta_{cs} - \delta_{as}(t_1)\\ &= \delta_{as}(t) - \delta_{as}(t_1) \approx m_{cs} + m_{as}(t) - \delta_{cs} - m_{cs} - m_{as}(t_1) + \delta_{cs}\\ &= m_{as}(t) - m_{as}(t_1) = \alpha \ln\left[1 + \frac{\beta}{\alpha}(t - t_r)\right]\\ &\quad - \alpha \ln\left[1 + \frac{\beta}{\alpha}(t_1 - t_r)\right] \approx \alpha \ln\left[\frac{\alpha + \beta t}{\alpha + \beta t_1}\right]\\ &\quad \text{for } t_1 \leq t \ll t_d = \frac{\alpha}{V_{pl}}, \end{aligned} \tag{A6}$$

that is the relation (3) of the main text.

SUPPORTING INFORMATION

Additional Supporting Information may be found in the online version of this article:

Section S1. Seismicity cluster division and determination of the geometries.
Section S1. Inversion method.
Section S3. Coseismic inversion.
Figure S1. Maps of the geometries tested, listed in Table 1. Black lines, green lines and GPS markers are the same of Fig. 1. All the faults are divided in $\sim 2 \times 2\,\mathrm{km}^2$ patches.
Figure S2. Temporal eigenvalues V for the decomposition of the coseismic data set. The decomposition with two components does not preserve more information on the coseismic offset than the decomposition with one component.
Figure S3. Example of outlier and blunder detection and removal in detrended and common mode error (CME) filtered time-series. The red line indicates the time-series obtained from the decomposition with one component. (a) shows the precleaning time-series of CONI, (b) the post-cleaning one.
Figure S4. Trade-off curve for the post-seismic inversion on the geometry P2, assuming a variable rake ($R = 1$) configuration. The figure shows the typical L-curve of the misfit (here χ^2) versus the roughness of the model ($\|G_{\mathrm{Lap}}L\|^2$). We choose the value indicated by the arrow, that correspond to a $\gamma = 2.5\,\mathrm{cm}^{-1}$.
Figure S5. χ^2 versus R curve for the post-seismic inversion on the geometry P2, assuming $\gamma = 2.5\,\mathrm{cm}^{-1}$, as derived from the trade-off curve with $R = 1$ (Fig. S4). The curve has a minimum for $R = 1$, since it is the configuration with no constraints on the rake. The increasing of the R parameter encourages slip distributions with larger dip components than strike ones. This constraint is translated in an increasing χ^2 value. For R, which tends to ∞, the curve reaches an asymptotic value. We choose the value $R = 15$.
Figure S6. Trade-off curve for the post-seismic inversion on the geometry P2 inverting for a slightly variable rake ($R = 15$). The figure shows the typical L-curve of the misfit (here χ^2) versus the roughness of the model ($\|G_{\mathrm{Lap}}L\|^2$). We choose the value indicated by the arrow, that correspond to $\gamma = 2.5\,\mathrm{cm}^{-1}$.
Table S1. Occupation history of the GPS stations used in this work. x-axis shows the time in days, where 0 is the mainshock epoch. Stations in bold style belong to continuous GPS networks; the other to survey mode networks.
Table S2. Column 1: station names. Column 2: offset calculated as the modelled value of the day after the mainshock less the modelled value of the day before. Column 3: as column 2, but with the decomposition values which are assumed as representative of the data. Column 4: error associated to the values of column 3. Column 5: difference between the offset obtained by the model and the offset of the decomposition. Column 6: ratio between the absolute value of columns 5 and 4. The values are referred to the east component of sGPS stations.
Table S3. As in Table S2, but the values are referred to the north component of sGPS stations.
Table S4. As in Table S2, but the values are referred to the vertical component of sGPS stations.
Table S5. As in Table S2, but the values are referred to the east component of cGPS stations.
Table S6. As in Table S2, but the values are referred to the north component of cGPS stations.
Table S7. As in Table S2, but the values are referred to the vertical component of cGPS stations (http://gji.oxfordjournals.org/lookup/suppl/doi:10.1093/gji/ggt522/-/DC1).

Please note: Oxford University Press is not responsible for the content or functionality of any supporting materials supplied by the authors. Any queries (other than missing material) should be directed to the corresponding author for the article.